Materials Horizons

REVIEW

Check for updates

Copper-based catalysts for the electrochemical reduction of carbon dioxide: progress and future prospects

Qingquan Kong, [ID] [ab] Xuguang An, [ab] Qian Liu, [b] Lisi Xie, [b] Jing Zhang, [ab] Qinye Li, [cd] Weitang Yao, [ID] [ab] Aimin Yu, [ID] [e] Yan Jiao [ID] [f] and Chenghua Sun [ID] *[d]

There is an urgent need for the development of high performance electrocatalysts for the CO_2 reduction reaction (CO_2RR) to address environmental issues such as global warming and achieve carbon neutral energy systems. In recent years, Cu-based electrocatalysts have attracted significant attention in this regard. The present review introduces fundamental aspects of the electrocatalytic CO_2RR process together with a systematic examination of recent developments in Cu-based electrocatalysts for the electroreduction of CO_2 to various high-value multicarbon products. Current challenges and future trends in the development of advanced Cu-based CO_2RR electrocatalysts providing high activity and selectivity are also discussed.

1. Introduction

Fossil fuels currently play an increasingly crucial role in global economic growth, technological progress and industry.[1,2] However, rapid worldwide economic development and population growth have led to the excessive utilization of conventional nonrenewable fossil fuels such as coal, petroleum and natural gas. This scenario has, in turn, significantly increased the concentration of carbon dioxide (CO_2) in the atmosphere, causing a series of global disasters and environmental problems such as global warming, desertification, ocean acidification, extreme weather and catastrophic floods.[3–7] Therefore, there is an urgent need to develop reliable and efficient methods of converting CO_2 into value-added chemicals and/or fuels with the goal of solving the above-mentioned crisis and achieving a sustainable carbon neutral society.

Reducing the level of CO_2 in the atmosphere while also converting CO_2 into valuable chemicals and/or fuels as a means

[a] *School of Mechanical Engineering, Chengdu University, Chengdu 610106, Sichuan, P. R. China*

[b] *Interdisciplinary Materials Research Center, Institute for Advanced Study, Chengdu University, Chengdu 610106, Sichuan, P. R. China*

[c] *Dongguan University of Technology, School Chemistry Engineering and Energy Technology, Dongguan 523808, P. R. China*

[d] *Department of Chemistry and Biotechnology, and Center for Translational Atomaterials, Swinburne University of Technology, Hawthorn, VIC 3122, Australia. E-mail: chenghuasun@swin.edu.au*

[e] *School of Science, Computing and Engineering Technology, Swinburne University of Technology, VIC, 3122, Australia*

[f] *School of Chemical Engineering and Advanced Materials, The University of Adelaide, Adelaide, SA 5005, Australia*

of realizing carbon neutral energy conversion could possibly be achieved by the capture, sequestration and utilization of this compound.[5,8–10] However, it is well known that CO_2 is a thermodynamically stable molecule with strong covalent bonds such that it is not readily converted into other compounds. The electrochemical CO_2 reduction reaction (CO_2RR) is a promising and environmentally friendly approach to converting CO_2 into valuable fuels and/or chemicals under ambient conditions. This process is therefore a potential solution to issues related to future energy shortages and could provide sustainable carbon-neutral energy conversion.[2,5,11–14] Although CO_2RR technologies have been studied since the early 19th century, it was not until 1985 that Hori *et al.* reported that CO_2 could be converted into methane (CH_4) as the major product along with various other compounds, including carbon monoxide (CO), formate ($HCOO^-$) and hydrocarbons on a variety of metal electrodes.[15] Since then, many studies have examined the development of advanced CO_2RR catalysts so as to increase the efficiency of the CO_2RR.

To date, many catalytic materials have been proposed as CO_2RR electrocatalysts on the basis of possessing high electrical conductivity and good intrinsic catalytic activity while being readily available. The carbon-based catalysts (*e.g.*, N-doped carbon, B- and N-co-doped carbon, Ru(II) polypyridyl carbene, graphene-based materials *etc.*) have shown the catalytic ability to electrochemically reduce CO_2 to a variety of hydrocarbons and oxides, but they usually suffering from low current densities, large overpotential, poor stability, as well as difficult to prepare at scale.[16,17] Among the potential metal-based catalytic materials candidates, Fe, Mn, Zn, Au, Ag, Pd and Ga have been

demonstrated to be highly efficient CO_2RR catalysts for the production of CO while Sn, Bi, Sb, In, Pb, Hg, Ti and Cd have been primarily used to generate liquid products such as formic acid (HCOOH) or $HCOO^-$. As an example, a wide variety of carbon-based compounds can be obtained using Cu-based electrocatalysts. These include C_1 products (*e.g.*, CO, HCOOH, methanol (CH_3OH) and CH_4), C_2 products (*e.g.*, ethylene (C_2H_4), acetaldehyde (CH_3CHO), acetate (CH_3COO^-) and ethanol (C_2H_5OH)) and C_{2+} products (*e.g.*, acetic acid (CH_3COOH), acetone (CH_3COCH_3) and *n*-propanol (C_3H_7OH)). Compared with C_1 products, the C_2 and C_{2+} products have higher energy densities and are more valuable and so currently play important roles in the energy supply and chemical industries.[10,18–27] However, Cu catalysts commonly suffer from high overpotentials and poor selectivity for the CO_2RR. In addition, the CO_2RR is a multi-component reaction process capable of generating up to 16 different products, such that it is difficult to use on an industrial scale.[28] Another issue identified by many studies is that the rate of the Cu-catalyzed CO_2RR rapidly decreases within several hours.[10,29] Therefore, it is imperative to develop advanced Cu-based electrocatalysts exhibiting high selectivity, improved activity and excellent stability while providing the desired reduction products.

In recent years, there has been considerable research with the aim of designing efficient Cu-based heterogeneous materials as CO_2RR electrocatalysts. These materials have comprised monometallic Cu, Cu-based oxides and other Cu-based compounds, Cu-based bimetallic systems, single/dual Cu atoms and Cu-based metal-organic frameworks (MOFs) among others.

The present review examines the performance of Cu-based catalysts along with the associated reaction mechanisms. The focus is on introducing fundamental aspects of the electrocatalytic CO_2RR after which the latest developments in the design of Cu-based electrocatalysts for the electroreduction of CO_2 to high-value multi-carbon products are systematically summarized. Lastly, unsolved challenges and anticipated future progress related to the development of advanced Cu-based CO_2RR electrocatalysts with high activity and selectivity are examined. It is the hope of the authors that this review will provide a comprehensive overview of recent developments in the study of Cu-based CO_2RR electrocatalysts.

2. Fundamental aspects of the electrocatalytic CO_2RR

2.1 Performance evaluation parameters, electrochemical cell configurations and electrolytes

2.1.1 Performance evaluation parameters.
The parameters that are commonly used to compare and evaluate the catalytic performances of CO_2RR systems include the overpotential (η), current density (j), partial current density ($j_{partial}$), faradaic efficiency (FE), turnover number (TON) and turnover frequency (TOF). The parameter η is the potential difference between the measured and theoretical potentials required to drive the CO_2RR and so a catalyst with superior CO_2RR activity will

typically exhibits a low η with respect to the generation of certain products. The value of η is calculated as

$$\eta = E - E_{eq}, \qquad (1)$$

where E is the measured electrode potential and E_{eq} is the standard potential for the formation of the product. The parameter j is the total current (i) per unit area (A) of the cathode electrode and is calculated as

$$j = i/A. \qquad (2)$$

The value of j indicates the overall rate of the CO_2RR and so this variable is an important aspect of evaluating the electrocatalytic activity of a catalyst. The parameter $j_{partial}$ for a given product can be obtained from the relationship

$$j_{partial} = FE \times j. \qquad (3)$$

Here, FE is calculated according to Faraday's Law and equals the ratio of the charge consumed by the formation of the product to the total charge (Q). This term is determined as

$$FE = znF/Q, \qquad (4)$$

where z is the number of electrons transferred, n is the amount of product in moles and F is Faraday's constant (96 485 C mol^{-1}). FE is used to describe the selectivity of the catalyst during the electrocatalytic reduction of CO_2. The TON is the yield of a product acquired using a unit amount of the catalyst while the TOF is the yield of a product generated using a unit amount of the catalyst over a unit time period. Both the TON and TOF are used to describe the electrocatalytic activity of the catalyst.

2.1.2 Electrochemical cell configuration.
The electrochemical cell structure is an important factor affecting the CO_2 reduction process and will determine the FE, current density and stability. Since Hori first reported the electrochemical reduction of CO_2 in the 1980s,[15] different electrochemical cells have been developed. At present, reactor vessels can be primarily divided into H-type, flow, solid-oxide electrolysis and differential electrochemical mass spectrometry cells (Fig. 1). It is worth noting that the CO_2RR is still in the laboratory research stage and the catalytic current density based on mass transport limitations is currently the primary factor preventing the commercial application of this technology. Therefore, further research is needed with regard to the design of more efficient electrochemical cells.

To date, commercially available H-type cells (Fig. 1a) are still the most common laboratory reactors for the CO_2RR. In these units, the working and reference electrodes are placed in the cathode compartment while the counter electrode is situated in the anode compartment.[30,31] The two compartments are usually connected by a circular channel and separated by an ion exchange membrane to prevent the oxidation of reduction products during the CO_2RR. Throughout the CO_2RR process, gaseous CO_2 continuously flows into the cathodic compartment through a conduit while the gas phase products are sampled and transferred to a gas chromatograph to determine the composition of the product mixture. It should be noted that the electrochemical cell must be airtight and the gas flow rate is
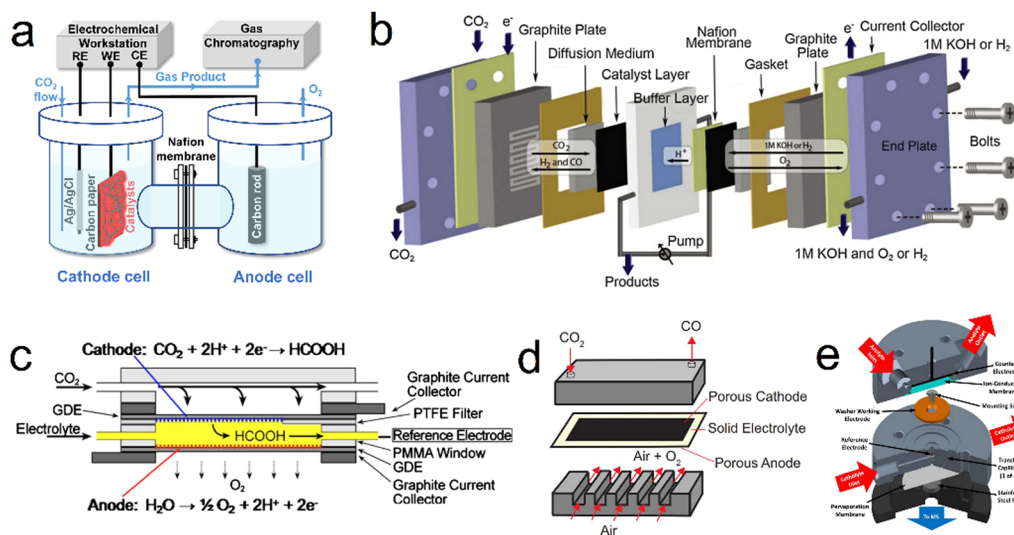
Fig. 1 Diagrams showing various electrochemical cell concepts. (a) H-Type. (b) PEM flow. (c) Microfluidic. (d) Solid-oxide electrolysis. (e) DEMS cells. Reproduction with permission from ref. 31, Copyright 2022, Chinese Chemical Society and Reproduction with permission from ref. 34, Copyright 2013, The Electrochemical Society and Reproduction with permission from ref. 35, Copyright 2013, The Electrochemical Society and Reproduction with permission from ref. 74, Copyright 2018, Cell Press and Reproduction with permission from ref. 37, Copyright 2022, American Chemical Society.

typically controlled by a mass flow meter at the inlet or outlet of the cell. In addition, liquid products are collected from the electrolyzed electrolyte and evaluated by nuclear magnetic resonance spectrometry or liquid chromatography-mass spectrometry. However, it should be noted that the concentration of each liquid product has to be above the detection limit of the analytical technique (either high performance liquid chromatography or liquid chromatography-mass spectrometry), which may not always be the case because the FE associated with most such products is very low. Therefore, longer electrolysis durations and smaller compartment volumes are recommended for the determination of such compounds in trials involving an H-type cell. In addition, although the H-type cell is widely used in the study of the CO₂RR, the relatively large distance between the counter and working electrodes, the low solubility of CO₂ in the electrolyte and the inherent mass transfer limitations in this system tend to produce low catalytic current densities ($j <$ 100 mA cm^{-2}), which greatly limits practical applications.

Various flow cell designs have been developed to increase the catalytic current density that can be obtained from the CO₂RR. In a typical flow cell, CO₂ is continuously supplied to the cathode using a gas diffusion electrode (GDE) or a system involving the external circulation of an electrolyte in which CO₂ is dissolved.[32,33] In contrast to an H-type cell, the reduction of CO₂ reduction at a GDE can remove the effect of mass transfer limitations and provide higher CO₂ concentrations on the catalyst surface, thus enabling higher catalytic current densities in such flow cells. The polymer electrolyte membrane (PEM) concept (Fig. 1b) is currently the most widely used type of CO₂ flow cell and has led to significant progress in the study of the CO₂RR.[34] The configuration of such units is almost the same as those of proton exchange membrane fuel cells and typically comprises a membrane electrode assembly, cathode/anode current collectors and cathode/anode flow plates. Because this

cell configuration contains only working and counter electrodes, without a reference electrode, adjustment of the current rather than the potential is often used to control the reaction, such that it can be challenging to differentiate anode and cathode degradation effects. The membrane electrode assembly, which is the most important component of such cells, consists of a cathode and anode, a GDE and a PEM. The electrodes are positioned close to one another such that the cell resistance is decreased. In a PEM flow cell, the catalysts are typically deposited on a carbon-based gas diffusion layer (made of either carbon paper or carbon cloth) to prolong the contact time with CO₂ while also providing a high surface area. Fig. 1c presents a diagram of a typical sandwich-structured microfluidic flow cell.[35] This reactor consists of two GDEs separated by a Nafion-117 membrane. During the CO₂RR, the electrolyte is injected into the cell at a specific flow rate selected to allow online collection of the reaction products for analysis. Importantly, the performance of such devices can be effectively improved by adjusting both cell parameters and reaction conditions, including the system pressure distribution, electrolyte flow rate, chamber/channel size and electrode structure.

In addition to electrochemical cells operating at room temperature such as those described above, solid oxide electrolysis cells (SOECs) can be used for CO₂ reduction at high temperatures (>873 K) (Fig. 1d). These devices have recently become of interest because they provide advantages such as improved reaction kinetics and reduced internal resistance, thereby achieving higher reaction efficiencies without using noble metal catalysts. A typical SOEC has three primary parts: a cathode for CO₂ reduction, an anode for oxygen evolution and a solid electrolyte for ion transport at temperature range from 300 °C to 1500 °C. In this cell configuration, the main product of the CO₂RR is CO, although coke and CH₄ are also produced. Despite the narrow range of products obtainable from such

systems, the product selectivity and catalytic performance of SOECs are generally superior to those of low temperature systems.[36]

Differential electrochemical mass spectrometry (DEMS) can continuously separate and collect electrochemical reaction products in real time based on pervaporation technology, followed by rapid analysis of these products (with an analysis time on the order of 1 s). In 2015, Clark and coworkers designed a novel DEMS cell (Fig. 1e) and demonstrated the applicability of this unit to the analysis of the electrochemical reduction of CO_2 on polycrystalline Cu.[37] In this DEMS cell a parallel working and counter electrode are separated by an ion-conducting membrane to ensure a uniform distribution of potential on the electrode surface and prevent unwanted parasitic reactions. During the CO_2RR, a CO_2-saturated electrolyte is pumped into the cell at a constant flow rate to supplement the CO_2 consumed by electroreduction while simultaneously providing efficient mass transfer to the cathode. The catholyte volume between the working electrode and pervaporation membrane is minimized to ensure that the delay time between product generation and detection is greatly shortened, with a delay on the order of 2 s. Products are delivered to a collection chamber and then efficiently assessed by mass spectrometry.

2.1.3 Electrolytes. The electrolyte acts as a conductive medium during the electrolysis process and the specific cations and anions in this medium can significantly affect the CO_2RR performance. The electrolytes employed for the CO_2RR can be divided into three categories: aqueous solutions, organic solvents and ionic liquids. The most common inorganic electrolytes used in aqueous solutions are sodium bicarbonate ($NaHCO_3$) and potassium bicarbonate ($KHCO_3$), which act as both proton donors and pH buffers. The addition of halide anions to the electrolyte has been found to have a positive effect on the CO_2RR, as demonstrated by reduced overpotentials and enhanced reaction rates.[38,39] In addition, the sizes of the cations and anions in the electrolyte can also affect CO_2RR performance.[40–43] Except bicarbonate, potassium hydroxide (KOH) electrolyte is also commonly used in CO_2RR. KOH electrolyte with high pH value is conducive to the electroreduction of CO_2, which may be due to the fact that anions are more easily adsorbed on the electrode surface or the anode potential is reduced in KOH electrolyte. Because CO_2 is more soluble in organic solvents than in aqueous solutions, electrochemical CO_2 reduction occurs more readily in organic solvents. The most commonly used organic solvents for the CO_2RR are propylene carbonate, dimethyl sulfoxide, *N,N*-dimethylformamide, acetonitrile and methanol. The liquid products produced by these solvents typically include formic acid, oxalic acid, glyoxylate and glycolate. Among these potential solvents, methanol is superior because of its relatively low toxicity and minimal cost together with its ability to provide high yields.[44]
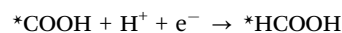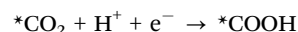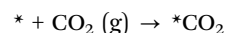
Ionic liquids are a class of molten salts having very low melting points. These compounds can also be employed in CO_2RR systems because they tend to exhibit wide electrochemical windows, good electrical conductivity, high CO_2 solubility and essentially nil vapor pressure.[45] Ionic liquids are generally thought to serve as co-catalysts in addition to solvents because they can reduce the generation of the CO_2 radical anion intermediate ($CO_2^{\bullet-}$), thus lowering the overpotential associated with CO_2 reduction.[46,47] Among the many ionic liquids, 1-ethyl-3-methylimidazolium tetrafluoroborate (EMIM-BF$_4$) is widely used because the moderate binding energy of EMIM with CO_2 promotes CO_2 reduction.[48]
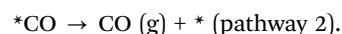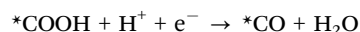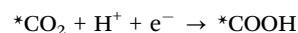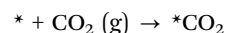
Modifying the electrolyte can also affect the electronic structure of the catalyst while also stabilizing Cu$^+$ ions during the reaction, representing another means of enhancing the CO_2RR. As an example, Yang *et al.* reported that the controlled surface reconstruction of commercial polycrystalline Cu could be readily accomplished using ethylenediamine tetramethylenephosphonic acid as an electrolyte additive, leading to a substantial improvement in the extent of CO_2 electroreduction to CH_4.[49]
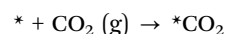
2.2 Reaction mechanism

The CO_2RR in an aqueous electrolyte involves proton coupled electron transfer. This is a complicated process comprising multiple single-step reactions and so a variety of reduction products are obtained. The mechanism by which such products are generated can be examined based on the specific carbon products that are formed. The most commonly reported C_1 products are CO, CH_4, HCOOH/HCOO$^-$ and CH_3OH. The formation of CO requires that adsorbed *CO_2 (where * indicates an active site) on the catalyst is initially reduced to generate *$CO_2^{\bullet-}$. Following this, the *$CO_2^{\bullet-}$ is converted to *COOH. In the case that this species then undergoes hydrogenation, HCOOH/HCOO$^-$ will be formed, representing pathway 1.[50] However, if dehydration occurs, gaseous CO is obtained, representing pathway 2.[51] The associated reaction pathways are
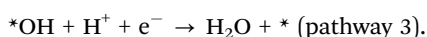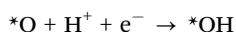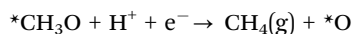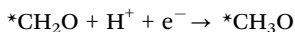
$$* + CO_2\,(g) \rightarrow {}^*CO_2$$

$$^*CO_2 + H^+ + e^- \rightarrow {}^*COOH$$

$$^*COOH + H^+ + e^- \rightarrow {}^*HCOOH$$

$$^*HCOOH \rightarrow HCOOH(l) + *\ (\text{pathway 1})$$

and

$$* + CO_2\,(g) \rightarrow {}^*CO_2$$

$$^*CO_2 + H^+ + e^- \rightarrow {}^*COOH$$

$$^*COOH + H^+ + e^- \rightarrow {}^*CO + H_2O$$

$$^*CO \rightarrow CO\,(g) + *\ (\text{pathway 2}).$$

If the *CO generated by pathway 2 does not desorb from the catalyst, it will be further reduced to *CHO, *CH_2O and *CH_3O with the eventual formation of CH_4, representing pathway 3.[51] This sequence can be summarized as

$$* + CO_2\,(g) \rightarrow {}^*CO_2$$

$$*CO_2 + H^+ + e^- \rightarrow *COOH$$

$$*COOH + H^+ + e^- \rightarrow *CO + H_2O$$

$$*CO + H^+ + e^- \rightarrow *CHO$$

$$*CHO + H^+ + e^- \rightarrow *CH_2O$$

$$*CH_2O + H^+ + e^- \rightarrow *CH_3O$$

$$*CH_3O + H^+ + e^- \rightarrow CH_4(g) + *O$$

$$*O + H^+ + e^- \rightarrow *OH$$

$$*OH + H^+ + e^- \rightarrow H_2O + * \text{ (pathway 3)}.$$
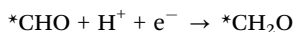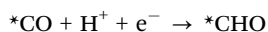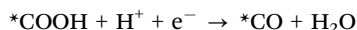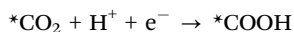
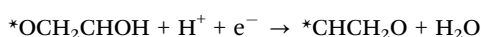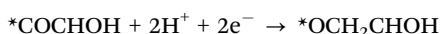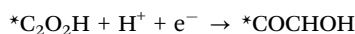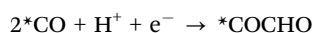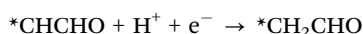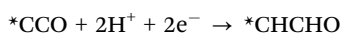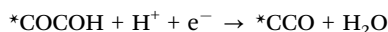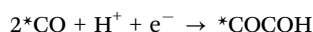According to Suzuki *et al.*, the rate-limiting step in the formation of CH_4 is $*CO \rightarrow *CHO$.[52] It should also be noted that CH_3OH is a side product of the CH_4 formation process.[50] The C_2 products from this process are typically C_2H_4 and C_2H_5OH and early research established that $*CO$ is a key intermediate in the formation of these two products.[53] If a dimerization reaction based on PCET between two $*CO$ takes place on the catalyst, the resulting $*C_2O_2H$ intermediate will lead to the formation of C_2 products. In the following step, the outgoing H^+ can bond with the α-carbon on $*C_2O_2H$ to produce C_2H_4 as the end product *via* pathway 4, which can be summarized as

$$2*CO + H^+ + e^- \rightarrow *COCHO$$

$$*C_2O_2H + H^+ + e^- \rightarrow *COCHOH$$

$$*COCHOH + 2H^+ + 2e^- \rightarrow *OCH_2CHOH$$

$$*OCH_2CHOH + H^+ + e^- \rightarrow *CHCH_2O + H_2O$$

$$*CHCH_2O + H^+ + e^- \rightarrow *CH_2CH_2O$$

$$*CH_2CH_2O \rightarrow C_2H_4(g) + *O \text{ (pathway 4)}.$$
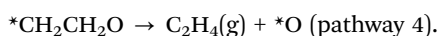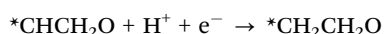
Another proposed mechanism of C_2H_4 production from CO_2RR has also been reported by Janik and Asthagiri (pathway 5):[54]
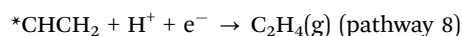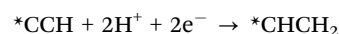
$$2*CO + H^+ + e^- \rightarrow *COCOH$$

$$*COCOH + H^+ + e^- \rightarrow *CCO + H_2O$$

$$*CCO + 2H^+ + 2e^- \rightarrow *CHCHO$$

$$*CHCHO + H^+ + e^- \rightarrow *CH_2CHO$$

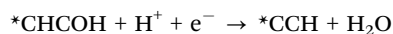$$*CH_2CHO + H^+ + e^- \rightarrow C_2H_4(g) + *O \text{ (pathway 5)}$$

If there is no loss of $*O$ after the generation of $*CH_2CHO$, the reaction will continue as follows (pathway 6):

$$*CH_2CHO + H^+ + e^- \rightarrow *CH_2CH_2O$$

$$*CH_2CH_2O + H^+ + e^- \rightarrow C_2H_4(g) + *O \text{ (pathway 6)}$$
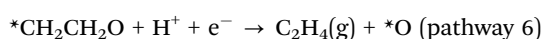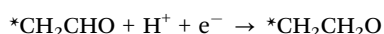
If there is no loss of $*O$ after $*CH_2CH_2O$ production, the reaction will continue as follows (pathway 7):

$$*CH_2CH_2O + H^+ + e^- \rightarrow *CH_3CH_2O$$

$$*CH_3CH_2O + H^+ + e^- \rightarrow C_2H_4(g) + *O + H_2O \text{ (pathway 7)}$$
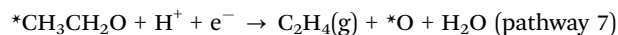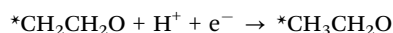
In addition, Goddard and coworkers found that when the $*COCOH$ intermediate is produced, C_2H_4 can be produced through another path (pathway 8):[55]

$$2*CO + H^+ + e^- \rightarrow *COCOH$$

$$*COCOH + H^+ + e^- \rightarrow *COHCOH$$

$$*COHCOH + 2H^+ + 2e^- \rightarrow *CHCOH + H_2O$$

$$*CHCOH + H^+ + e^- \rightarrow *CCH + H_2O$$

$$*CCH + 2H^+ + 2e^- \rightarrow *CHCH_2$$

$$*CHCH_2 + H^+ + e^- \rightarrow C_2H_4(g) \text{ (pathway 8)}$$
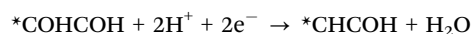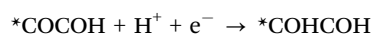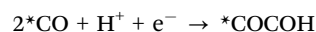
After the formation of $*C_2O_2H$ intermediate, if the proton bonds with the β-carbon of $*C_2O_2H$, the final product is C_2H_5OH *via* the reaction sequence:

$$2*CO + H^+ + e^- \rightarrow *C_2O_2H$$

$$*C_2O_2H + H^+ + e^- \rightarrow *C_2O + H_2O$$

$$*C_2O + H^+ + e^- \rightarrow *C_2OH$$

$$*HC_2O + H^+ + e^- \rightarrow *CHCHO$$

$$*CHCHO + H^+ + e^- \rightarrow *CH_2CHO$$

$$*CH_2CHO + H^+ + e^- \rightarrow *CH_3CHO$$

$$*CH_3CHO + H^+ + e^- \rightarrow *CH_3CH_2O$$

$$*CH_3CH_2O + H^+ + e^- \rightarrow *CH_3CH_2OH$$

$$*CH_3CH_2OH \rightarrow CH_3CH_2OH(l) + * \text{ (pathway 9)}.$$
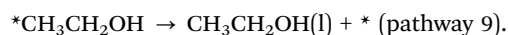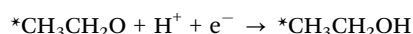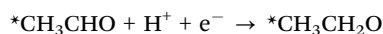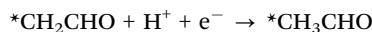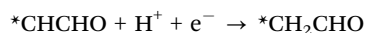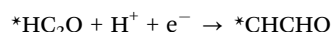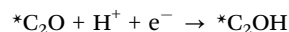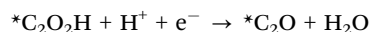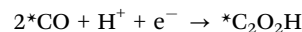
Another proposed mechanism of CH_3CH_2OH generation is reported as follows (pathway 10):[55]

$$2*CO + H^+ + e^- \rightarrow *COCOH$$

$$*COCOH + H^+ + e^- \rightarrow *COHCOH$$

$$*COHCOH + 2H^+ + 2e^- \rightarrow *CHCOH + H_2O$$

$$*CHCOH + H^+ + e^- \rightarrow *CHCHOH$$

$$*CHCHOH + H^+ + e^- \rightarrow *CH_2CHOH$$

$$*CH_2*CHOH + H^+ + e^- \rightarrow *CH_3CHOH$$

$$*CH_3CHOH + H^+ + e^- \rightarrow CH_3CH_2OH(l) \text{ (pathway 10)}$$
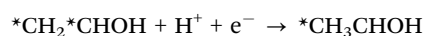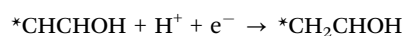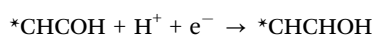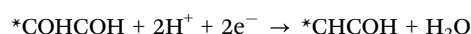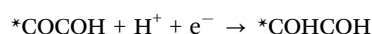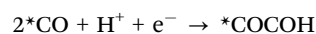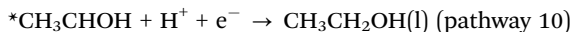
Bell and Head-Gordon found that CH_3CH_2OH can be produced *via* another pathway (pathway 11):[56]

$$2*CO + H^+ + e^- \rightarrow *COCHO$$

$$*COCHO + H^+ + e^- \rightarrow C_2H_2O_2 \text{ (glyoxal)}$$

$$C_2H_2O_2 + 3H^+ + 3e^- \rightarrow *CH_2CHO$$

$$*CH_2CHO + H^+ + e^- \rightarrow *CH_3CHO$$

$$*CH_3CHO + H^+ + e^- \rightarrow *CH_2CH_2OH$$

$$*CH_2CH_2OH + H^+ + e^- \rightarrow CH_3CH_2OH(l) \text{ (pathway 11)}$$
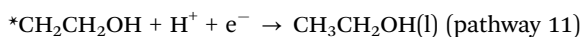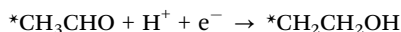
CH_3COOH is another possible C_2 product but, as a consequence of the associated energy barriers and multiple proton-electron transformations, only a few electrocatalysts are capable of efficiently reducing CO_2 to CH_3COOH.[57–59]

The reaction sequence for this mechanism is

$$* + CO_2 \text{ (g)} \rightarrow *CO_2$$

$$*CO_2 + H^+ + e^- \rightarrow *COOH$$

$$*COOH + H^+ + e^- \rightarrow *CO + H_2O$$

$$*CO + H^+ + e^- \rightarrow *CHO$$

$$*CHO + H^+ + e^- \rightarrow *CH_2O$$

$$*CH_2O + H^+ + e^- \rightarrow *CH_3O$$

$$*CH_3O + H^+ + e^- \rightarrow *CH_3OH$$

$$*CH_3OH + H^+ + e^- \rightarrow *CH_3 + H_2O$$

$$*CH_3 + CO_2(g) \rightarrow *CH_3COO$$

$$*CH_3COO + H^+ + e^- \rightarrow *CH_3COOH \text{ (pathway 12)}.$$
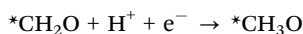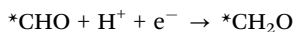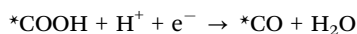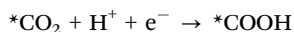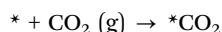
For the CH_3COOH formation route, $*CH_3$ on the active site is a critical intermediate. If dimerization of $*CH_3$ is occurred instead of the reaction with $*CO$, ethane will be formed.[2,60]

The formation of C_3 products such as propanol[61] and acetone[62] is also sometimes observed during the CO_2RR process although the associated mechanism remains unclear and the FE values for these products are less than 25%. It is assumed that the insertion of C_1 species into stabilizing C_2 intermediates is an important step in the generation of C_3 products such as *n*-propanol.[63] Highly efficient catalysts are needed to improve the selectivity and yields of C_3 products.

Theoretical investigations (*e.g.*, Density Function Theory (DFT) calculations) could provide vital support to the experimental results and predicting the product selectivity as well as the mechanistic insights in the case of electrocatalysts.[64–68]

Garza *et al.* propose a reaction mechanism for the reduction of CO_2 to C_2 products over a copper electrode using DFT calculations combined with experimental findings.[56] Additionally, theoretical modeling can also accelerate the rational design of catalysts compared to traditional experimental studies. Scaling relationships and some activity descriptors including the d-band center for the transition-metal surface and the valence state of metals have been successfully established,[69–71] which correlate the simple parameters of catalysts with complex catalytic performance, lead to develop excellent electrocatalysts. Recently, Wang *et al.* develop a simple universal descriptor $\left(\varphi = (\chi_M + \sum \chi_x) + N_{d/p}\right)$ to assess the catalytic performance of 2D material-supported dual-atom catalysts (DACs@2D) for electrochemical reduction based on first-principles calculations, the conservation of the orbital symmetry, and feature engineering *via* the machine-learning method.[72] This descriptor is closely correlated with inherent atomic properties such as electro-negativity (χ), electron type and number ($N_{d/p}$). On this basis, $CuCr/g-C_3N_4$ for CH_4 and $CuSn/N-BN$ for $HCOOH$ with extremely low onset potentials of -0.24 and -0.11 V have been identified.
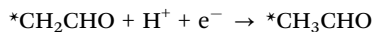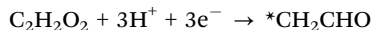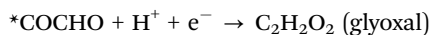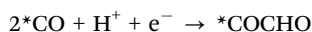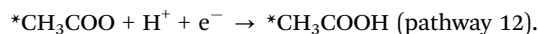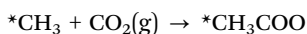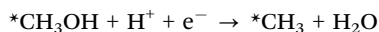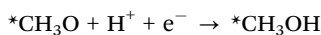
2.3 Practical applications

Many products obtained from the CO_2RR (such as CO, $HCOO^-$, C_2H_4, ethanol and propanol) have important usage in modern industrial processes. Consequently, the practical applications of the CO_2RR could have significant economic benefits. To thoroughly evaluate the industrial cost of practical products from CO_2RR, the involved technologies such as CO_2RR process, catalyst preparation, electrolyzer design, and the separation, purification and storage of product have to be taken into consideration. Due to the current CO_2RR technology remains far from the level of maturity required for industrialization, we can screen out promising products from CO_2RR process for practical application at the present stage. FE is widely considered as the primary standard to assess the practical application potential of CO_2RR products.[73] An outstanding FE means high selectivity of a specific product, which can significantly decrease the cost of product separation and purification. For a high FE product, its economic benefits can be calculated from the difference between the market price of raw materials and the electricity cost of per mol product.[73] As an example, assuming a cost of electricity on an industrial scale of \$0.05 kW h^{-1}, the price of ethanol obtained from the electroreduction of CO_2 would be on the order of \$0.32 L^{-1},[74] which is much less than 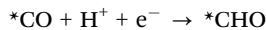the fuel ethanol price of \$1.51 L^{-1} in 2022. According to the product selectivity and economic benefits of various CO_2RR products, CO, HCOOH, ethanol, and ethene show high potential of industrial application. At the moment, the electroreduction of CO_2 to CO is the most promising technology for practical applications and has been demonstrated at the pilot plant level. Haldor Topsoe built the world's first CO_2-to-CO plant based on solid oxide electrolysis cells in 2017, capable of producing from 10 to 100 N m^3 of gaseous CO per hour with a purity of 99.5%.[75] In addition, in 2020, Schmid *et al.* set up an aqueous CO_2-to-CO electrolyzer system with a power rating of approximately 300 W to pursue

industrialization and achieved a CO production efficiency above 90% with an operating lifetime of over 1500 h.[76] Based on reported CO_2-to-CO plant or pilot plant test,[58–61] the involved technical indicator for industrial application should be current density $\geq$ 500 mA cm^{-2}, FE $\geq$ 90%, CO concentration in product gas $\geq$ 30%, purity of purified CO $\geq$ 99.5%, cell size in a square-meter range, and stability $\geq$ 1000 h. The industrial scale production of other CO_2RR products will require significant progress before industrialization but the discovery of more efficient catalysts, electrolytes and electrolyzers could lead to the practical synthesis of these compounds *via* the CO_2RR.

3. Cu-Based electrocatalysts for the CO_2RR

3.1 Monometallic Cu

The synthesis of single-carbon products such as CO and CH_4, as well as higher value-added C_{2+} hydrocarbons, alcohols and oxygenates, has attracted much attention. In particular, techno-economic analyses of possible CO_2RR products have shown that C_{2+} products such as C_2H_4 and ethanol provide a reasonable balance between value and preparation difficulty. Although the synthesis of such compounds shows great potential, the energy conversion and chemical transformation efficiencies of the CO_2RR are presently limited by the lack of efficient electrocatalysts. In addition, because of the unique value for the binding energy between the *CO intermediate and Cu, this is the only metal capable of catalyzing C–C coupling to form C_{2+} products at reasonable rates.[77] Unfortunately, polycrystalline Cu is unselective and can generate up to 16 different products, which is extremely inconvenient with regard to the implementation of this process on an industrial scale.[78] This section reviews the factors that can potentially affect the catalytic performance of copper. The effects of the Cu structure, including surface crystalline facets and grain boundaries, are initially examined, followed by an assessment of the viability of defect engineering and geometric structure regulation.

3.1.1 Facets. Polished Cu polycrystalline foils having primarily exposed (111) facets have been shown to catalyze C–C coupling for the formation of C_{2+} products. However, the associated FE values are often much lower than those for the generation of C_1 products such as HCOOH, CO and CH_4.[28] Analyses of the structure-property relationships of single crystals have established that the selectivity of a Cu catalyst is determined by the degree of crystallinity of the Cu. Early work by Hori comprised the systematic assessment of the performance of 19 single-crystal Cu surfaces at different applied potentials and demonstrated the structure-sensitive nature of the CO_2RR.[79] Specifically, the reduction of CO_2 at Cu(100) facets affords C_2H_4 instead of CH_4 whereas oxygenated hydrocarbons such as acetaldehyde, ethanol and acetic acid are the primary compounds obtained from Cu(110).[54,79] Wang *et al.* studied the effects of particular Cu facets on the initial C–C coupling steps during CO_2 reduction using DFT calculations and suggested that both Cu(100) and stepped facets favor C_{2+}

product formation compared with Cu(111).[80] Wang's group also developed a metal ion cycling method to synthesize single crystalline Cu_2O nanocubes having primarily Cu_2O(100) facets. These oxide nanocubes could be subsequently reduced to polycrystalline Cu nanocubes with preferentially exposed Cu(100) facets for efficient C–C coupling. Sargent *et al.* proposed a strategy based on the *in situ* electrodeposition of Cu under CO_2 reduction conditions that preferentially exposed and maintained Cu(100) facets and therefore favored the formation of C_{2+} products.[81] More recently, Gong *et al.* described the effect of the facets of Cu crystals derived from Cu(OH)$_2$, CuO or Cu_2O as precursors on the CO_2RR.[82] The Cu catalysts obtained from Cu(OH)$_2$ had relatively high densities of exposed Cu(110) and Cu(100) steps assembled into Cu(210) and Cu(310) facets. These materials also exhibited improved activity during the CO_2RR to generate C_{2+} products based on the promotion of CO adsorption and C–C coupling. Consequently, superior selectivity for C_{2+} products, a high FE of 87% and a large partial current density of 217 mA cm^{-2} for C_{2+} products have been achieved at a voltage of only -0.54 V *vs.* a reversible hydrogen electrode (RHE; the reference for all potentials in this article unless otherwise specified) in a flow-cell electrolyzer in alkaline aqueous solutions.

Compared with Cu(100) facets, the high-index Cu(511), Cu(711), Cu(911), Cu(11,1,1), Cu(310), Cu(510), Cu(610) and Cu(810) facets provide even higher C_2H_4-to-CH_4 ratios with greater overall C_{2+} selectivity.[83–85] These high-index facets can be visualized as combinations of terraces and steps on low-index facets that maximize the contribution of active sites. Work with such materials provides a means of assessing the synergistic effects between different facets and eventually improving the selectivity beyond theoretically predicted limitations.[85] Huang *et al.* reported the preparation of activated Cu nanowires (A-CuNWs) with highly active stepped surfaces (assigned to A-(*hkl*)) through an *in situ* electrochemical activation process (Fig. 2a). These materials were found to contain increasing proportions of A-(*hkl*) after prolonged activation durations, suggesting that the {100} and {110} facets expressed on the synthesized CuNWs surfaces were gradually transformed into the higher-energy A-(*hkl*) surface structures during the electrochemical activation process. As the proportion of the stepped A-(*hkl*) surfaces was gradually increased from 0 to 40.68%, the FE for C_2H_4 production underwent a corresponding increase from 47.04% to 71.19% (Fig. 2b and c). These A-CuNWs also demonstrated exceptionally high stability over a time span of approximately 200 h.[84] DFT calculations demonstrated that the thermodynamically favored Cu(511) plane [3(100) $\times$ (111)] stepped surface provided a higher energy barrier for the C_1 path and also slowed the hydrogen evolution reaction (HER) such that the selectivity for C_2H_4 was greatly increased (Fig. 2d–g). Guo *et al.* very recently investigated the C–C coupling process on Cu stepped surfaces based on *ab initio* molecular dynamics (AIMD) and density functional theory (DFT) calculations and established the nature of CO–CO adsorption sites, indicating that the high selectivity for C^{2+} products could ascribe to the high-index facet.[86]

3.1.2 Grain boundary engineering. Grain boundary (GB) engineering is another important strategy for enhancing the
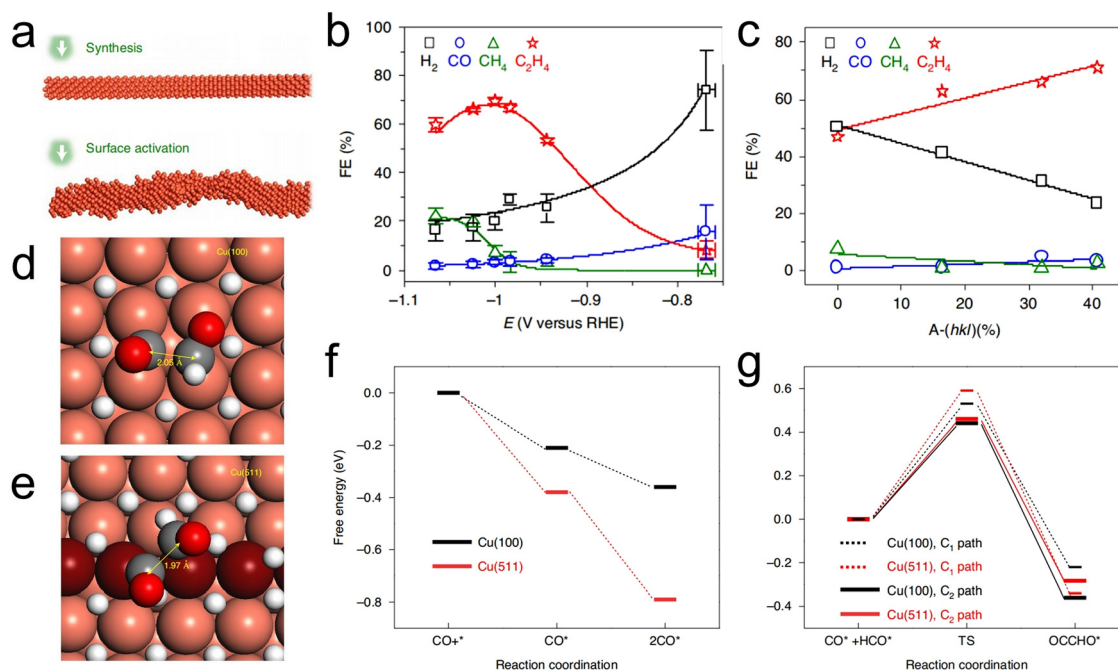
Fig. 2 (a) A diagram showing the preparation of Cu NWs with surface activation step, (b) the FE of A-CuNW at various potential, (c) the correlations between FE values and A-(hkl) over the approximate range of −0.99 to −1.00 V (*vs.* RHE). Transition states determined for the C$_2$ pathway on (d) Cu(100) and (e) Cu(511). (f) CO and 2CO adsorption energies (ΔG_{ads}) on Cu(100) and Cu(511) and (g) C$_1$ and C$_2$ pathways on Cu(100) and Cu(511). Reproduction with permission from ref. 84, Copyright 2020, Springer Nature.

catalytic activity during the CO$_2$RR. In 2012, Li *et al.* reported the application of Cu electrodes prepared by the electrochemical reduction of oxidized Cu foil (OD-Cu) for CO$_2$ reduction.[87] An OD-Cu-500 (annealed at 500 °C) specimen was found to provide peak FE values of approximately 45% and 38% at approximately −0.3 and −0.5 V with regard to CO and HCOO$^-$ production, respectively. At overpotentials higher than −0.5 V, both FEs decreased dramatically and were essentially nil at −1.0 V. Simultaneously, the selectivity for hydrocarbon products slowly increased, although only C$_2$H$_4$ and ethane were obtained, both with FE values of less than 10%. As a consequence of such studies, there has been much interest in determining the mechanisms responsible for the enhanced reduction currents and FE values associated with nanostructured Cu electrodes.

Subsequent studies determined that OD-Cu electrodes possess abundant GBs and identified a linear correlation between GB density and CO$_2$RR performance.[88,89] Raciti and Wang reported systematic investigations of high density Cu nanowires applied to the CO$_2$RR.[90,91] Electrocatalytic experiments showed that these materials were highly active during the electrochemical reduction of CO$_2$ and selectively generated CO at low overpotentials (more positive than −0.5 V) but C$_2$ species (ethane, C$_2$H$_4$ and ethanol) at more negative potentials. Interestingly, positive and negative correlations were observed between catalytic performance and high-angle and coherent GBs, respectively. Gong *et al.* generated realistic OD-Cu surface models by simulating the "oxide-derived" process based on molecular dynamics with global neural network potential coupled as well as density functional theory calculations and experimental verification.[92] This work identified three square-

shaped sites that were likely to be responsible for C–C coupling. Among these, planar-square and convex-square sites associated with Σ3 GBs were found to be responsible for C$_2$H$_4$ production while step-square sites (*i.e. n*(111) × (100)) favored the synthesis of alcohols.

Liu *et al.* established that dual catalytic pathways on adjacent active motifs of Cu GBs were responsible for enhanced C$_{2+}$ production using first principles calculations.[93] Fig. 3a presents GB models with Cu(100) facets built according to the coincidence site lattice theory. In these models, the d-band center of GB sites is closer to the Fermi level than that of Cu(100) facets and the Cu atoms at GBs have shorter bond lengths and stronger bonding with *CO. This would be expected to enhance the adsorption of *CO at GBs. The pathways for the two different C–C coupling modes to produce C$_2$H$_4$ (Fig. 3b) indicate that the CO$_2$RR at GBs does indeed proceed *via* a tandem reaction mechanism (Fig. 3c). This work provided an improved understanding of the CO$_2$RR at GB surfaces and suggested a new approach to overcoming the limitations of the structure-performance relationship of single sites on Cu(100) facets.

3.1.3 Defect engineering. Defect engineering based on twin boundaries, stacking faults and stepped sites can be used to optimize the adsorption, enrichment and confinement of reaction intermediates and hydroxyl ions on electrocatalysts to improve electrocatalytic performance.[94–96] Choi *et al.* reported the high-yield synthesis of star-shaped decahedron Cu nanocrystals having high densities of twin boundaries and stacking faults (Fig. 4a and b).[94] The presence of these crystal defects evidently increases the *CO binding energy but significantly decrease the energy barrier to the formation of *CHO, a common
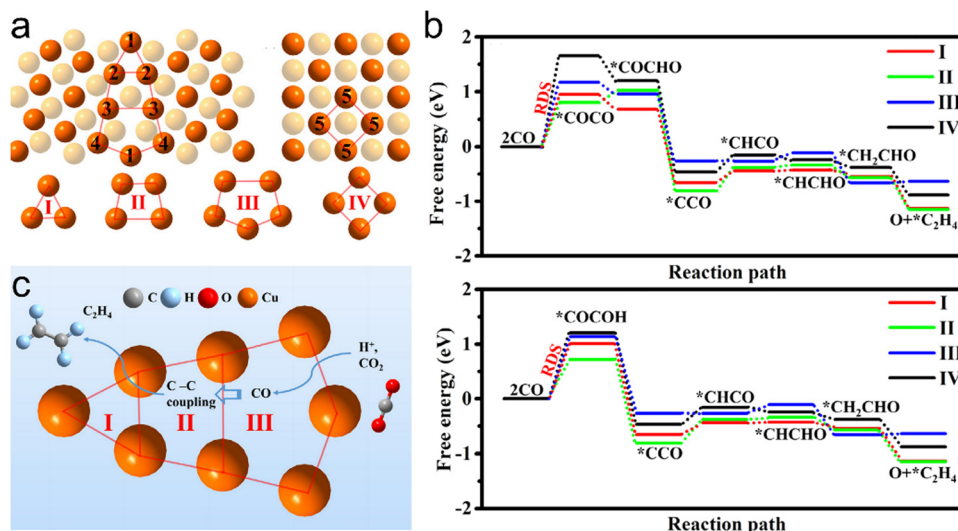
Fig. 3 (a) Cu atom structures of R5{021}/[100]GB and (100) facets, (b) the reaction pathways from CO_2 to C_2H_4 based on (top) C–C coupling *via* *COCO as an intermediate and (bottom) C–C coupling *via* *COCOH as an intermediate. (c) Diagram of the cascade reaction of C_2H_4 between different sites on a GB surface. Reproduction with permission from ref. 93, Copyright 2022, Elsevier.

intermediate for both CH_4 and C_2H_4 generation. Consequently, multiple-twinned nanocrystals displayed a low overpotential for CH_4 synthesis, such that the onset potential was lowered by 0.149 V relative to the value obtained using polycrystalline commercial Cu nanoparticles. In addition, high selectivity for C_2H_4 production was observed, with an FE of 52.43% at −0.993 V *vs.* RHE (Fig. 4c). Zhang *et al.* designed Cu nanosheets having nano-scaled defects with sizes of 2–14 nm for the electrochemical production of C_2H_4 from carbon dioxide.[95] As shown in Fig. 4d and the enlarged HAADF-STEM image in Fig. 4e, each nanosheet contained numerous pits. On the basis of the high density of atomic defects that concentrated crucial adsorbates (*CO, *OCCO and OH⁻) required for C–C coupling, nanodefective Cu nanosheets provided a record C_2H_4 FE of 83.2% and a high current density of −60 mA cm⁻² at −1.18 V *vs.* RHE (Fig. 4f).

Interestingly, CO-rich environments have been used to construct Cu catalysts with stepped sites that result in high surface coverages of *CO intermediates and bridge-bound *CO adsorption. These effects, in turn, trigger CO_2 reduction pathways that form alcohols rather than C_2H_4. A FE value of 70% and high current densities over 100 mA cm⁻² during the synthesis of C_{2+} alcohols in an H-cell system were obtained on this basis (Fig. 4g–i).[96]

3.1.4 Geometric structure regulation. The efficiency with which multi-carbon products are obtained using Cu-based catalysts can be improved by optimizing *CO adsorption and reducing the energy barrier for C–C coupling. Liu *et al.* reported that a strong local electric field can be obtained by regulating the arrangement of Cu nanoneedle arrays (CuNNAs).[97] According to finite element simulations and the results of DFT calculations, CuNNAs with vertically ordered tip arrangements should exhibit a stronger tip local electric field compared with randomly distributed nanoneedles (CuNNs), leading to localized K⁺ accumulation and stronger *CO adsorption, thus reducing the C–C coupling energy barrier. On the basis of these theoretical predictions, the same group prepared vertically ordered CuNNAs and randomly disordered CuNNs on Cu foil by template-assisted electrodeposition (Fig. 5a). CO_2 reduction performance tests indicated that the CuNNAs provided an FE of 59% for multi-carbon products at −1.2 V vs RHE compared with 20% for the CuNNs (Fig. 5b). The very high localized electric fields produced by the ordered CuNN arrays evidently promoted the accumulation of K⁺ ions and this effect enhanced both *CO adsorption and C–C coupling (Fig. 5c). Biener *et al.* demonstrated that Cu catalysts synthesized by electron beam (EB) exhibit excellent current densities, selectivities and energy efficiencies. This superior performance can be ascribed to the faceted surface morphologies and narrow Cu/gas diffusion layer interfaces of such materials, which increase their hydrophobicity (Fig. 5d and e).[98]

3.1.5 Cu clusters and amorphous nanoparticles. Atomically-precise Cu clusters with high surface/volume ratios and more active sites have attracted attention with regard to the CO_2RR process.[99–101] Dong *et al.* reported that Cu_{79} clusters (where the subscript indicates the number of Cu atoms in the cluster) provide a lower energy barrier for CO_2 reduction to CO than the values for bulk Cu (111) and (211) surfaces.[99] Similarly, Cu_{20} clusters show superior selectivity during the CO_2RR with an improved ability to prevent the HER. The Cu atoms at the vertices and edges on Cu_{20} cluster surfaces are potential active sites for CO_2 reduction to HCOOH.[100] Very recently, Zang *et al.* developed structurally precise Cu_8 cluster isomers having different core structures (either cubes or ditetrahedra). The ditetrahedron-shaped Cu_8 clusters exhibited a high FE_{HCOOH} of approximately 92% at −1.0 V.[101]

Amorphous NPs possess low-coordinated surface atoms with dangling bonds that can serve as reactive sites for catalysis.[102,103] Yan *et al.* achieved the first-ever tunable synthesis of either amorphous or crystalline Cu nanoparticles (having sizes on the order of 3 nm) in a similar reaction environment and explored their catalytic performance during the CO_2RR.[103] The
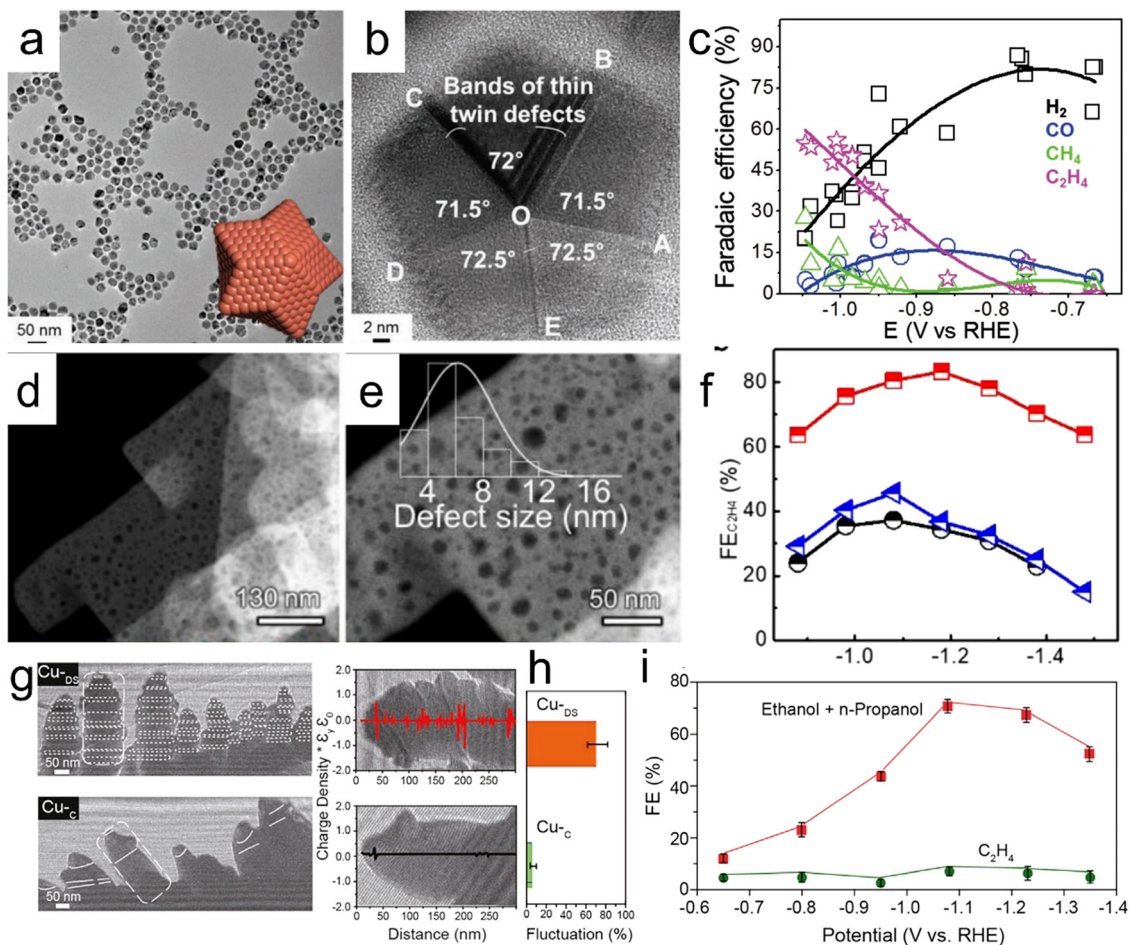
Fig. 4 (a) Low-magnification TEM image of SD-Cu NPs (the inset shows a theoretical atomic structure), (b) an HRTEM image of SD-Cu NPs demonstrating fivefold twin symmetry, (c) FE values of SD-Cu NPs as functions of E, (d and e) HAADF-STEM images of a n-Cu NS sample (the inset in (e) shows the size distribution of the nano-defects on the material), (f) C_2H_4 FE values at various applied potentials for n-CuNS, CuNS and CuNP, (g) electron holographs of Cu-DS and Cu-C, (h) charge density signal fluctuations and (i) FE values for Cu-DS and Cu-C under different potentials. Reproduction with permission from ref. 94, Copyright 2019, Wiley-VCH and Reproduction with permission from ref. 95, Copyright 2020, American Chemical Society and Wiley-VCH and Reproduction with permission from ref. 96, Copyright 2021, Cell Press.

amorphous Cu NPs exhibited superior CO_2RR performance, achieving a total FE for liquid fuels of 59% at −1.4 V, with HCOOH and C_2H_6O accounting for 37% and 22%, respectively, of the total products. The superior performance of amorphous Cu can be ascribed to the larger electrochemical active surface area (ECSA) of this material along with enhanced CO_2 adsorption. The reactive sites provided by regularly arranged atoms with short-range order are capable of binding and stabilizing the *CO intermediate and so facilitate the production of liquid fuels. This work suggested new techniques for improving the electroreduction of CO_2 based on the use of amorphous metal catalysts.

3.2 Cu-Based oxides

The oxidation state of the Cu in a catalyst can affect the activity and selectivity of the material during the CO_2RR by promoting reactant activation, regulating the adsorption of intermediates and facilitating the C–C coupling step.[104] Using DFT calculations, Goddard and co-workers showed that the synergy between Cu^+ and Cu^0 can promote CO_2 activation.[105] Specifically, the C atom of

CO absorbed at a Cu^+ site is positively charged whereas the C atom at a Cu^0 site will be negatively charged because of the back donation effect. Sargent and co-workers tuned the Cu oxidation state from −0.1 to +0.3 and found that the CO adsorption energy increased monotonically with increases in the oxidation number.[106] DFT calculations by the same group established that the presence of Cu^+ species favors dimerization.[107]

Over the past several years, several efficient Cu-based oxide catalysts have been developed that effectively inhibit the HER while improving both selectivity and reactivity during the CO_2RR. The oxidation state of the metal can affect the intrinsic performance of such catalysts by affecting structure and other properties, including spin state, work function, active sites and energy band structure.[104] Kanan et al. showed that the pre-oxidation of Cu can greatly increase its ability to promote C^{2+} formation.[87] Yu et al. also found that oxygen in OD-Cu catalysts plays a critical role in CO adsorption and dimerization.[108] DFT calculations indicated that oxygen on the Cu surface promotes
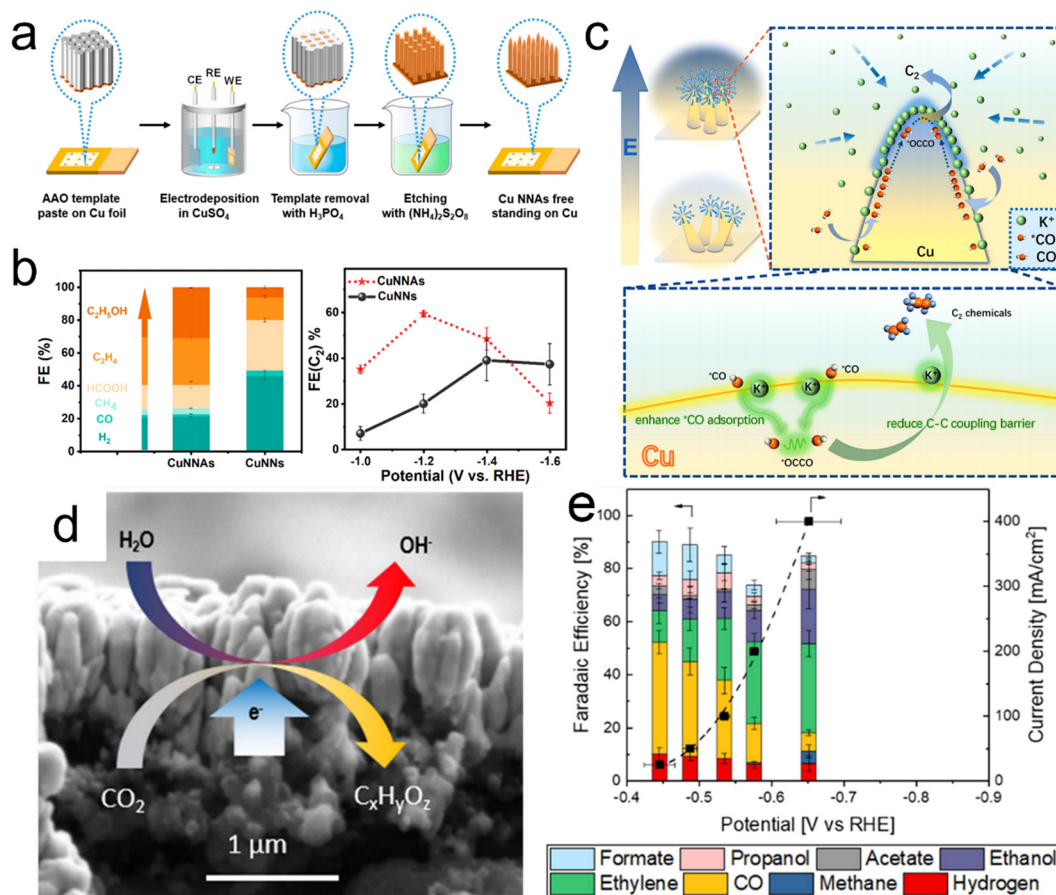
Fig. 5 (a) Diagram showing the synthesis of CuNNAs, (b) product distributions obtained from CuNNAs and CuNNs at −1.2 V *vs.* RHE together with FE(C$_{2+}$) values at different potentials, (c) diagram showing C$_{2+}$ formation on the single tip of a CuNNA. (d and e) Electron beam image of a Cu catalyst and corresponding FE values at different potentials. Reproduction with permission from ref. 97 and 98, Copyright 2022, American Chemical Society.

both CO adsorption and dimerization and so enhances the C–C coupling reaction. Following this work, various OD-Cu catalysts were developed by generating Cu structures using an anodic treatment[109] or O$_2$ plasma and these materials exhibited outstanding CO$_2$RR activity.[110]

It should be noted that tuning the relative proportions of Cu^0 and Cu$^+$ species is also a useful approach to obtaining better CO$_2$RR performance. Wu and co-workers synthesized three Cu electrodes with adjustable oxidation states of either Cu$^+$ or Cu^0 based on electrochemical deposition.[111] A Cu electrode subjected to cyclic voltammetry (CV) was found to contain both Cu^0 and Cu$^+$ species that synergistically catalyzed CO$_2$ reduction to generate C$_2$H$_4$ as a consequence of the dimerization of CO. This electrode exhibited a 40% FE for C$_2$H$_4$ at −1 V *versus* RHE. As shown in Fig. 6a, the relative proportions of Cu^0 and Cu$^+$ present during the CO$_2$RR can be tuned by regulating the anodic pulse potential (E_a) and anodic pulse time (t_a).[112] Using E_a = 0.6 V *versus* RHE and t_a = 1 s, Cu$_2$O species were formed on a Cu surface at a proportion of 16% and remained at a proportion of 7% throughout the CO$_2$RR. under these pulsed conditions, the Cu catalyst was able to convert CO$_2$ to C$_{2+}$ products with an FE of 76% at −1.0 V *vs.* RHE (Fig. 6b). Oxygen vacancies have also been demonstrated to act as

catalytic sites capable of promoting CO$_2$ activation and C$_1$ adsorption to generate C$_{2+}$ products. In a prior study, a Cu oxide with surface oxygen vacancies created by electrochemical reduction showed a FE of approximately 63% for the conversion of CO$_2$ to C$_2$H$_4$ (Fig. 6d and e).[113]

The above results indicate that the presence of Cu$^+$ promotes the formation of C$_{2+}$ products although it is not yet clear if the active oxide phase is present at the catalyst surface under the harsh CO$_2$RR conditions. Strasser *et al.* studied the synthesis of a (001)-oriented CuO nanosheet CO$_2$RR catalyst.[114] Operando X-ray absorption spectroscopy (XAS) studies confirmed the chemical reduction of CuO and concomitant formation of disordered and coordinatively under-saturated Cu^0 over a duration of approximately 2 h using reductive CO$_2$RR conditions. These undercoordinated sites were thought to be responsible for the high C$_{2+}$ production rates over this material. Using an electrochemical flow cell that allowed for *in situ* X-ray absorption spectroscopy (GIXAS) and X-ray diffraction (GIXRD) with improved CO$_2$ mass transfer, Drisdell *et al.* successfully demonstrated that surface Cu oxide was reduced to metallic Cu prior to the onset of the CO$_2$RR and that metallic Cu was the only detectable phase during the reaction.[115] Very recently, Cui *et al.* combined *in situ* Raman spectroscopy, secondary ion mass spectrometry and isotope-

Fig. 6 (a) Atomic force microscopy images of a Cu(100) electrode after different surface treatments and reaction settings, (b) product selectivity of the aforementioned surfaces under potentiostatic (−1.0 V) or pulsed conditions (product selectivity for t_c = 0.5 s is also included for comparison). The selectivity data reported here are averages of at least three diff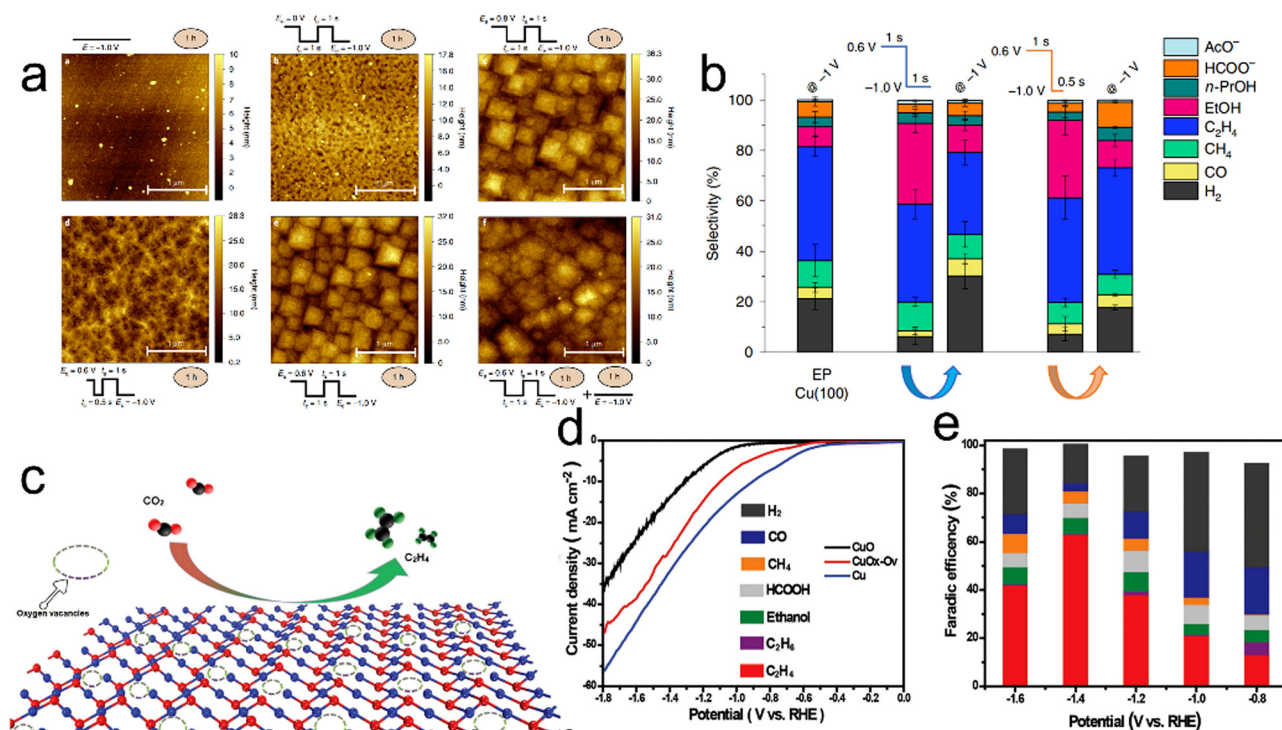erent measurements and the error is given as the standard deviation. (c) Diagram showing the electrocatalytic reduction of CO_2 to C_2H_4 on a Vo-rich CuO_x–Vo surface, (d) LSV curves for CuO_x–Vo, CuO and Cu in a CO_2-saturated 0.1 M KHCO$_3$ electrolyte and (e) FE values of CuO_x–Vo, at various potentials in CO_2-saturated 0.1 M KHCO$_3$. Reproduction with permission from ref. 112, Copyright 2020, Springer Nature and Reproduction with permission from ref. 113, Copyright 2019, Wiley-VCH.

labelling to demonstrate a "seesaw-effect" between the cathodic reduction and reoxidation induced by OH$^\bullet$ radicals and determine the chemical state and proportion of Cu$^{\delta+}$ species during the CO_2RR.[116] It is evident that the evolution and preservation of Cu$^{\delta+}$ species during the CO_2RR should be studied in more detail in future work.

To date, various strategies have been developed to maintain the Cu valence state during the CO_2RR, including the use of heteroatoms,[106] interface engineering[117,118] and coordination polymers.[119] Sargent and co-workers introduced boron as a dopant to tune the ratio of Cu$^{\delta+}$ to Cu^0 active sites and achieved an FE of approximately 80% for C_2 products at −1.1 V *vs.* RHE.[106] In addition, Yan *et al.* reported that the Cu oxidization state can be stabilized by introducing strong electronic interactions to suppress electron accumulation around the Cu$^+$ sites.[118] Yan's group proposed a model catalyst based on depositing Cu$_2$O nanoparticles onto hexagonal boron nitride (h-BN) nanosheets, and this material showed a 1.62-fold larger C_2H_4/CO ratio compared with bare Cu$_2$O. Theoretical calculations indicated that electrophilic h-BN received some electron density from Cu$_2$O and that this phenomenon strengthened the Cu–O bonds and stabilized the Cu$^+$ species in the catalyst.

3.3 Cu-Based compounds

Cu-containing compounds such as sulfides, phosphides and selenides contain modified active Cu sites and so often exhibit outstanding CO_2RR catalysis.[63,120–125] Hod *et al.* developed a Cu$_2$S catalyst for the CO_2RR using a cation change method (Fig. 7a).[121] The presence of S heteroatoms in this material changed the electronic structure of adjacent Cu sites, resulting in the presence of oxidized Cu$^+$ sites based on the higher electronegativity of S. These positively charged Cu sites were able to bind CO_2 to relatively electronegative oxygen, leading to the formation of *OCHO serving as the primary intermediate for the production of HCOO$^-$. The sulfur-modified Cu catalyst provided HCOOH in 0.1 M NaHCO$_3$ with an FE as high as 87.3% and record-high activity at −0.9 V *vs.* RHE (Fig. 7b). Sargent and coworkers reported the use of DFT calculations to show that the application of modified Cu$_2$S cores having Cu surface vacancies could cause the C_{2+} reaction pathway to transition from the formation of C_2H_4 to the generation of multi-carbon alcohols.[122] This same group synthesized a Cu$_2$S–Cu–V (where V denotes a vacancy) nanoparticle structure based on the controllable introduction of vacancies on a Cu surface shell having a Cu sulfide core, leading to FE values for C_3H_7OH and C_2H_5OH of 8 ± 0.7% and 15 ± 1% with partial current densities of 2.5 ± 0.1 and 4.8 ± 0.1 mA cm^{-2} at −0.95 V *vs.* RHE, respectively.

In addition, CuS has been reported to electrochemically reduce CO_2 to provide HCOOH (FE = approximately 60%)[123] or CH$_4$ (FE = approximately 73%) as the major product.[124] The selectivity of this material can be tuned based on its morphology and the local electronic structures of Cu atoms around sulfur atoms.
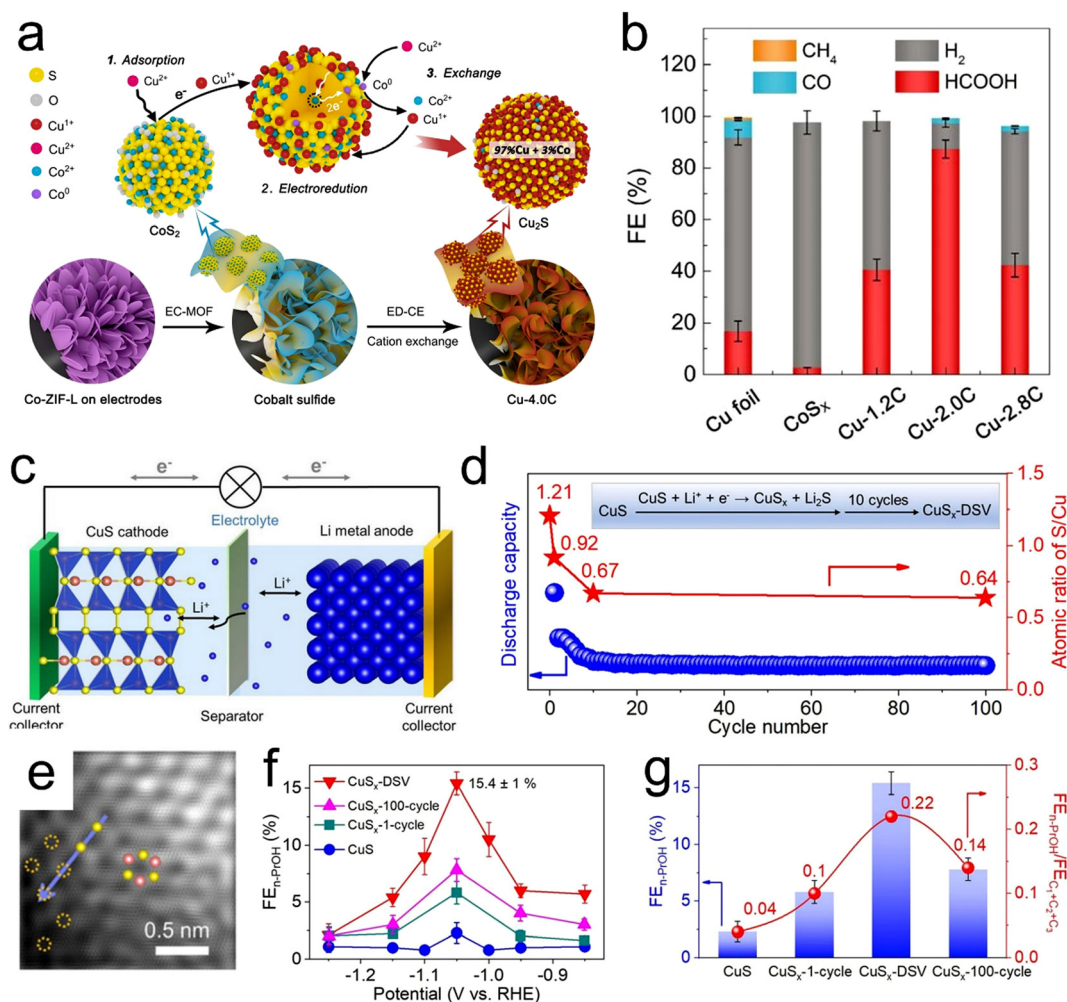
Fig. 7 (a) Diagram of the experimental paths and mechanisms for electrochemically-driven cation exchange, (b) FE values for CO_2RR products using Cu foil, CoS_x, Cu-1.2C, Cu-2.0C and Cu-2.8C at -0.9 V (vs. RHE). (c) Diagram of a lithium-ion battery assembled with CuS (cathode) and Li metal (anode), (d) discharge capacities of CuS (blue dots) and the S/Cu atomic ratios (red stars) with respect to the cycle number at a constant current of 0.044 mA cm^{-2} in the voltage range of 0.01–3 V. Sulfur atoms in the CuS lattice were selectively removed to form Li_2S, resulting in CuS_x-DSV. (e) HAADF–STEM image of CuS_x-DSV and (f and g) FE and FE$_{n-PrOH}$ values together with FE$_{n-PrOH}$/FE$_{C_1+C_2+C_3}$ ratios for n-propanol on four catalysts (CuS, CuS_x-1-cycle, CuS_x-DSV and CuS_x-100-cycle) at different applied potentials. Reproduction with permission from ref. 121, Copyright 2020, Wiley-VCH and Reproduction with permission from ref. 63, Copyright 2021, Springer Nature.

Recently, Zheng et al. synthesized CuS with double sulfur vacancies using an electrochemical lithium tuning strategy (Fig. 7c–e). This material enabled the stabilization of *CO and *OCCO dimers and CO–OCCO coupling to form the key *C$_{2+}$ intermediate for n-propanol.[63] As shown in Fig. 7f and g, the FE for n-propanol production was increased to 15.4% in H-cells and the partial current density for n-propanol production was further increased to 9.9 mA cm^{-2} in flow cells. This value was comparable to the performance reported for prior optimized electrochemical CO_2RR systems.

Transition metal selenides have also been widely applied as electrocatalysts owing to their low cost and unique physico-chemical properties. Han et al. provided the first report that Cu selenides exhibit outstanding performance during the conversion of CO_2 to methanol with a high FE of 77.6% and a current density of 41.5 mA cm^{-2} at a low overpotential of 285 mV.[126] Hu et al.

found that the bimetallic compound $CuInSe_2$ had Au-like catalytic properties with good CO_2RR and poor HER activity and could serve as an electrocatalyst for the highly selective CO_2RR to give CO with much greater efficiency than monometallic selenides.[127] Se vacancies evidently promoted the delocalization of electrons in this material and further optimized the CO_2RR to give an FE for CO production of 91% in aqueous solutions.

Dismukes et al. reported the synthesis, surface structure, electronic structure and catalytic activity of highly crystalline single-phase Cu_3P (on which [00I] facets were primarily exposed) when applied to the electrochemical reduction of CO_2 to formic acid.[125] It was suggested that the Cu$^+$ oxidation state was insufficient to achieve high CO_2RR activity and that close multi-Cu sites were essential to produce C$_2$ or larger products. The formation of a surface hydride at isolated *H-CuP$_3$ sites was thought to provide catalytic sites forming

both H_2 and $HCOO^-$ while the long Cu–Cu bonds inhibited the formation of C–C coupling products.

Most recently, Qiao *et al.* have reported reliable ampere-level CO_2-to-C_{2+} electrolysis on heteroatom engineering on Cu catalysts.[128] Among various Cu-based compounds with heteroatom (N, P, S, O), N-engineered Cu (N–Cu) catalyst exhibits the best CO_2-to-C_{2+} productivity, it achieves a C_{2+} partial current density of -909 mA cm^{-2} at -1.15 V, outperforms most reported Cu-based catalysts. Combined with *in situ* spectroscopy and density functional theory studies, indicating that the high adsorption strength of *CO on N–Cu results from the depressed HER and promoted *CO adsorption on both bridge and atop sites of Cu, which greatly reduces the energy barrier for C–C coupling.

3.4 Cu-Based bimetallic materials

Cu-Based bimetallic compounds have emerged as another class of CO_2RR electrocatalysts. The presence of a secondary metal near Cu can promote the efficiency of CO spillover and induce localized increases in interatomic distances. In addition, the ability to adjust the binding energies of adsorbates and intermediates can allow the formation of C_{2+} liquid products.[129] Cu-based bimetallic catalysts such as Cu–Pd, Cu–Au, Cu–Ag, Cu–Co and Cu–Zn alloys have been developed and demonstrated to show promise activity for the CO_2RR.[130–134] In prior work, Kenis *et al.* synthesized bimetallic Cu–Pd catalysts with different elemental mixing patterns, such as ordered, disordered and phase-separated. Diagrams of these materials and
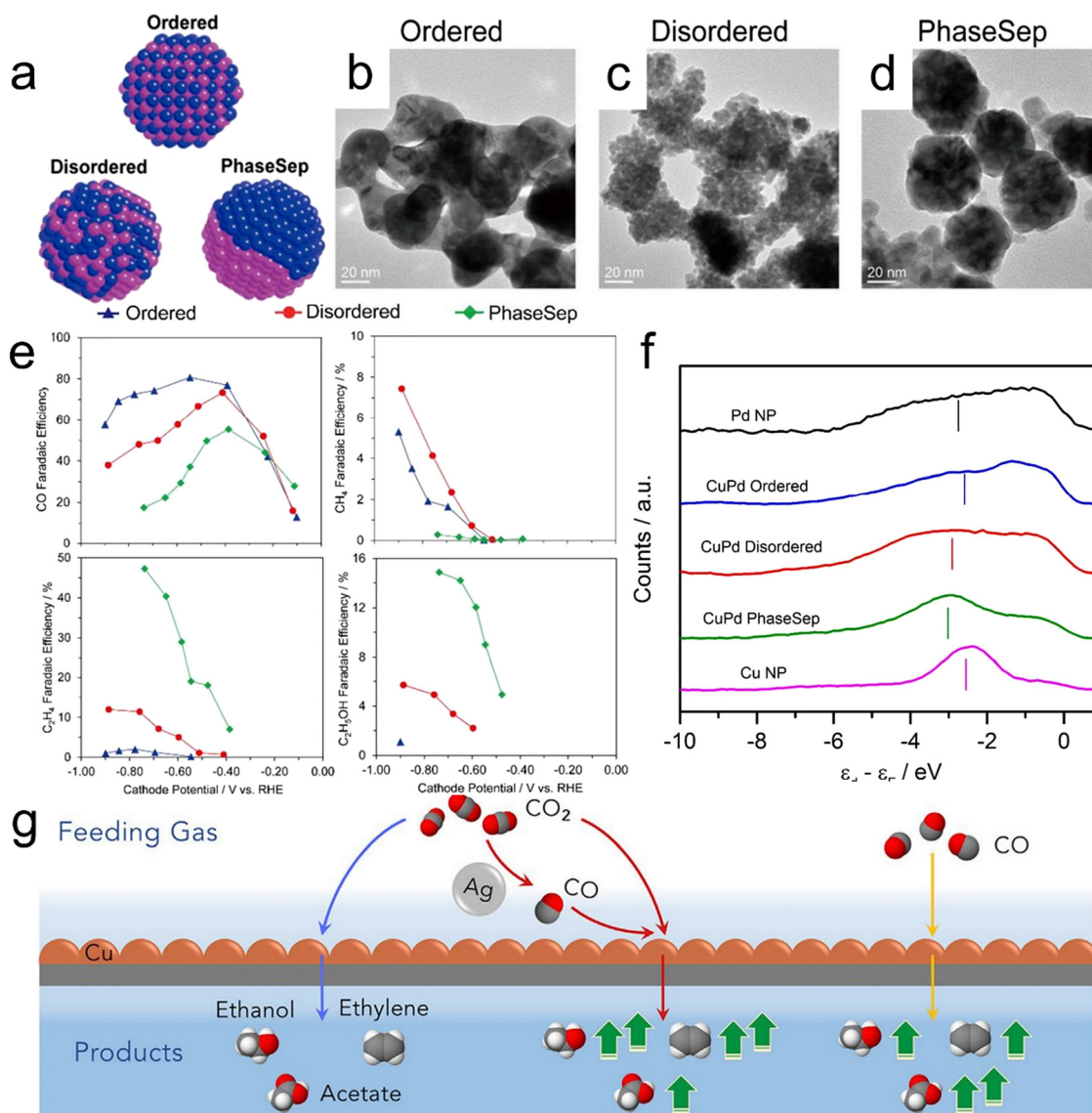
Fig. 8 (a) Diagrams of CuPd nanoalloys with different structures, (b–d) high-resolution TEM images of CuPd nanoalloys, (e) faradaic efficiencies for CO, CH_4, C_2H_4 and C_2H_5OH obtained using bimetallic Cu–Pd catalysts with different mixing patterns, (f) surface valence band photoemission spectra of CuPd nanoalloys relative to the Fermi level. (g) A diagram summarizing the catalytic systems provided by the local environments produced by a Cu–Ag tandem catalyst (red) and the standard CORR (yellow) or CO_2RR (blue). Reproduction with permission from ref. 130, Copyright 2017, American Chemical Society and Reproduction with permission from ref. 135, Copyright 2020, Cell Press.

corresponding high-resolution TEM images are presented in Fig. 8a–d.[130] A specimen having neighboring Cu atoms (that is, a phase-separated material) favored the production of C_{2+} products while that featuring an alternating Cu–Pd arrangement (a disordered structure) promoted the formation of CH_4 (Fig. 8e). Fig. 8f confirms that phase-separated Cu–Pd will have the lowest d-band center while Cu nanoparticles will have the highest. Even so, phase separated Cu–Pd and Cu nanoparticles show similar catalytic selectivity and activity, indicating that geometric/structural effects play a more important role in catalytic selectivity and activity than electronic effects.

Cuenya et al. explored the effect of metal composition and particle size on activity during the CO_2RR over well-defined CuCo NPs.[132] The FE and partial current density data confirmed that small amounts of Co enhanced the activity of these NPs while an increase in particle size favored the CO_2RR over the HER. Under CO_2RR conditions, the NPs underwent the surface segregation of Cu together with possible sintering, leading to a contraction of the Cu–Cu interatomic distance that weakened the binding energy between the surface and the key intermediates *COOH, *CO and *H. These structural and compositional changes have also been found to occur in CuZn nanoparticles. In such materials, metallic Cu in close proximity to ZnO leads to the production of CH_4 during the initial stage or the reaction, after which the progressive reduction of ZnO occurs under CO_2RR conditions. The simultaneous enhancement of Cu–Zn interactions and formation of a brass alloy later change the selectivity to exclusively generate CO and H_2.[133]

In addition to Pd, Cu can also be doped with Co, Zn and Ag for the efficient conversion of CO_2 to C_{2+} products. A Cu–Ag tandem catalyst has been found to enhance the C_{2+} production rate by promoting CO_2 reduction to CO on Ag and subsequent carbon coupling on Cu (Fig. 8g).[135] With the addition of Ag, the C_{2+} partial current over the Cu surface increased from 37 to 160 mA cm^{-2} at −0.70 V vs. RHE in 1 M KOH, indicating that the localized CO-enriched environment generated by Ag promoted C_{2+} formation on Cu. Very recently, He et al. used E-beam evaporation to synthesize a series of CuAg films with uniform distributions and controllable stoichiometries. A series of $Cu_{1-x}Ag_x$ ($x = 0.05–0.2$) alloys were found to suppress the formation of HCOOH, thus increasing the ratio of C_2 liquid products (such as ethanol and acetate) to the C_1 liquid product (HCOOH).[136] Moreover, an Au/Cu bimetallic catalyst was reported to exhibit improved activity and selectivity for C_{2+} alcohols at ambient temperature and pressure.[137] A tandem catalysis mechanism was proposed by Jaramillo et al. based on a combination of electrochemical testing and mass transport modelling. In this mechanism, CO_2 reduction on gold nanoparticles generates a high local concentration of CO on the neighboring Cu surface and this CO is then reduced to alcohols such as ethanol and n-propanol under locally alkaline conditions.

Various sp-block non-noble metals such as In,[138] Sn[139] and Sb[140] have previously been identified as highly selective electrocatalysts for CO_2 reduction. Alloying these non-noble metals with Cu to form Cu–In,[141,142] Cu–Sb[143] and Cu–Sn[144,145] has been found to promote CO formation while inhibiting the HER. As an example, Sun et al. demonstrated that Cu_2Sb-decorated Cu nanowire arrays on Cu foil could serve as highly active and selective electrocatalysts for the conversion of CO_2 to CO.[143] Trials in CO_2-saturated 0.1 M $KHCO_3$ achieved a high FE of 86.5% for CO at −0.90 V vs. RHE with an onset potential observed for CO evolution of −0.50 V vs. RHE and complete suppression of HCOO$^-$ formation. The unique spike-like microstructure obtained by alloying Cu with Sn atoms can also tune the electronic structure of the catalyst and so balance the adsorption and protonation of the *CO_2 intermediate while increasing the local electric field to raise the CO_2 concentration.[145] Porous $Cu_{6.26}Sn_5$ exhibits superior selectivity for HCOO$^-$ with an FE of $97.8 \pm 2.4\%$.

3.5 Single/dual Cu atom catalysts

Metal-based single atomic catalysts (SACs) and dual atom catalysts combine the merits of both heterogeneous and homogeneous catalysts with unique geometric and electronic characteristics. The advantages of these materials include low coordination of metal atoms, high atomic utilization and strong metal–support interaction,[146] all of which provide outstanding performance during the CO_2RR.[147–149] In this section, Cu SACs based on different support materials (such as oxides, nano-sized carbons and MXenes) as well as Cu-containing dual-atom catalysts with applications to electrochemical CO_2 conversion are considered.

The different coordination environments around isolated Cu atoms and the substrate play an important role in determining the products obtained from the CO_2RR. He et al. proposed a facile strategy for the large-scale synthesis of single-atom Cu-decorated through-hole carbon nanofibers (CuSAs/TCNFs).[150] In this work, metal atoms embedded in the self-supporting through-hole structure of the material were reduced to generate abundant single atoms of Cu capable of effectively catalyzing the CO_2RR, leading to a high partial current density of −93 mA cm^{-2} for C_1 products. This catalyst also remained stable for more than 50 h in an aqueous solution. According to DFT calculations, single Cu atoms provide a relatively high binding energy for the *CO intermediate, allowing this intermediate to be further reduced to products such as methanol rather than being released as CO. Zheng et al. demonstrated a facile approach to tuning active Cu sites for CO_2 electroreduction to form different hydrocarbons based on pyrolyzing MOF precursors at different temperatures.[7] The presence of nitrogen in these materials enabled good dispersion and attachment of atomic Cu species on nitrogen-doped carbon frameworks with Cu–N_x configurations. DFT calculation results indicated that these catalysts could produce C_2H_4 via the binding of two CO intermediates on adjacent Cu–N_2 sites. In addition, the isolated Cu–N_4, neighboring Cu–N_4 and isolated Cu–N_2 sites would all be expected to promote the formation of CH_4. Pyrrolic-N_4 sites were determined to provide the free energy required for the formation of the *COOH intermediate and for C–C coupling more readily than pyridinic-N_4 sites.[151] Recently, Zhu et al. reported the first synthesis of a carbon-dots-based SAC containing unique CuN_2O_2 sites and indicated that this material

showed a remarkably high FE of 78% and selectivity of 99% for CO_2RR products during the electrochemical conversion of CO_2 to CH_4 with a current density of 40 mA cm^{-2} in aqueous electrolytes (Fig. 9a–e).[152] Theoretical calculations also established that the high selectivity and activity at CuN_2O_2 active sites could be attributed to the optimally increased energy barriers to CH_4 and H_2 formation as well as to the fine-tuned electronic structure of the active Cu sites.

In addition to carbon-based materials, C_3N_4, metal oxides and MXenes have also been utilized as substrate materials for Cu SACs.[153–156] As an example, Zheng *et al.* developed a Cu-doped CeO_2 electrocatalyst with highly effective catalytic sites for the electroreduction of single CO_2 molecules to CH_4.[153] The strong interaction between CeO_2 and Cu in this material promoted the formation of single-atom dispersed Cu species as well as the surrounded multiple oxygen vacancies, and these effects were the primary cause of the excellent CH_4 selectivity shown by this catalyst. In this work, Cu–CeO_2-4% nanorods

provided a CH_4 FE of approximately 58% at –1.8 V *vs.* RHE. This study also demonstrated the rational design of highly dispersed metal catalytic centers at the single atom level with the aim of promoting the CO_2RR. Li *et al.* found that the loading of Cu SAs onto Al_2O_3 and Cr_2O_3 (acting as Lewis acids) significantly improved the rate of CO_2 reduction to CH_4 (Fig. 9f–h). A Cu/Al_2O_3 SAC exhibited a high selectivity of 62% towards CH_4 with a corresponding current density of 153.0 mA cm^{-2} at -1.2 V *vs.* RHE.[157] This work provided useful techniques for tailoring the electronic structure of Cu single atoms for the highly efficient CO_2RR.

MXenes having OH, O and F surface terminations have received much attention owing to the excellent electrical conductivity, chemical stability and abundant active catalytic sites of these materials.[158,159] As a result, MXenes have been widely employed as substrates for SACs. Sun *et al.* reported that Cu single atoms anchored on $Ti_3C_2T_x$ MXene nanosheets can act as effective and robust catalysts for electrochemical CO reduction,
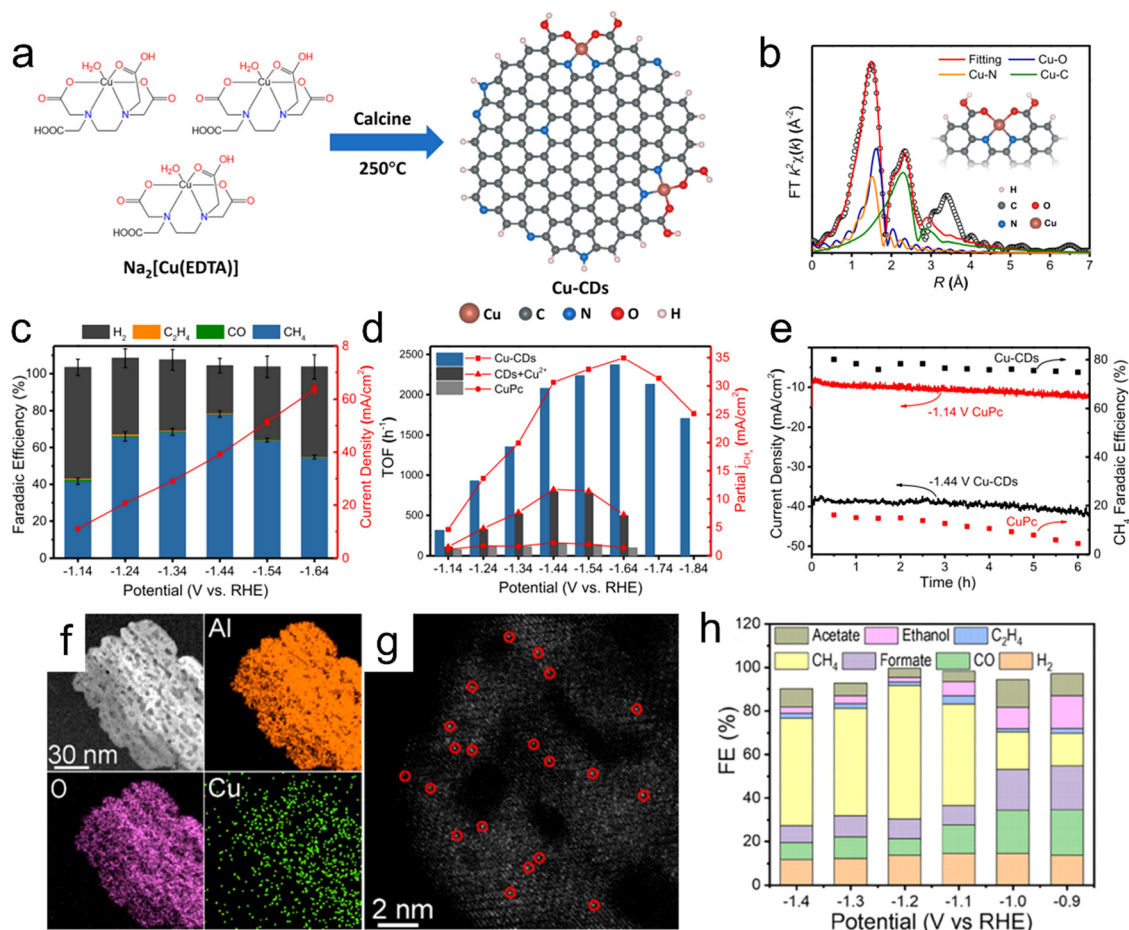
Fig. 9 (a) Diagram showing the low-temperature calcination of Cu-CD catalysts, (b) EXAFS fitting curves for Cu-CDs in *R* space based on the backscattering paths of Cu–N, Cu–O and Cu–C (the inset in (b) shows the structure of Cu sites in Cu-CDs), (c) dependence of FE (left *y*-axis) and current density (based on geometric surface area, right *y*-axis) of Cu-CDs on potential, (d) partial CH_4 current density plots and TOFs of Cu-CDs, CDs + Cu^{2+} and CuPc at different applied potentials, (e) stability test of Cu-CDs and CuPc at their highest CO_2RR FE potentials. (f and g) EDS elemental mapping images and aberration-corrected HAADF-STEM image (atomically-dispersed Cu is highlighted in red circles) of the Cu/p-Al_2O_3 SAC and (h) FE values for various products using the Cu/p-Al_2O_3 SAC. Reproduction with permission from ref. 152, Copyright 2021, Springer Nature and Reproduction with permission from ref. 157, Copyright 2021, American Chemical Society.

achieving an ultrahigh selectivity of 98% for the formation of multi-carbon products.[154] As an example, a high FE of 71% for C_2H_4 was obtained at -0.7 V vs. RHE. Theoretical simulations suggested that atomically dispersed Cu–O_3 sites favor the C–C coupling of CO molecules to generate the key *CO–-CHO intermediate and also lower the energy barrier associated with the potential rate-determining step. Yang et al. subsequently reported an efficient approach to producing single Cu atoms immobilized on MXene that exhibited a high FE value of 59.1% for CH_3OH and showed good electrocatalytic stability.[155] Single-atom Cu with an unsaturated electronic structure ($Cu^{\delta+}$, $0 < \delta < 2$) provided a low energy barrier for the rate-determining step (the conversion of *HCOOH to the absorbed *CHO intermediate) that was responsible for the efficient electrocatalytic reduction of CO_2 to CH_3OH.

The construction of paired atom structures to form dual atom Cu catalysts has also been proposed as a potentially useful means of modifying the catalytic behavior of atomic sites and increasing electrocatalytic performance.[149] Based on the position of the atoms, these dual atom catalysts are classified as either isolated or binuclear. Chen et al. demonstrated the first fabrication of a novel Ni–Cu atomic pair configuration with binuclear dual-atom sites with the aim of obtaining improved CO_2RR performance.[160] The incorporation of Cu in this system positively shifted the Ni 3d orbital energy to the Fermi level and thus accelerated the rate-determining step (*COOH formation). During the electrocatalytic CO_2RR, it is difficult to obtain a low overpotential because of scaling effects, by which increased *CO adsorption is always accompanied by stronger binding of *CHO (or *COH).[69] Wang et al. reported that this scaling relationship could be avoided to obtain efficient CO_2 electrochemical reduction by employing heteronuclear transition metal dimers embedded in a monolayer of C_2N as dual active centers.[161] In such systems, the binding energies of key reduction intermediates are completely decoupled so that the overpotential limitation no longer exists. CuCr/C_2N and CuMn/C_2N have exhibited the best performance among these materials to date, with very low limiting potentials (-0.37 and -0.32 V, respectively) for CH_4 production.

3.6 Cu-Based MOFs

MOFs have large specific surface areas and highly dispersed unsaturated metal centers that can be used as electrocatalysts. The catalytic performance of an MOF can also be tailored by tuning its structure, including the types of ligands and metals, degree of porosity and pore sizes and size distribution.[162] The first research regarding the electrocatalytic reduction of CO_2 utilizing a Cu-MOF was conducted in 2012.[163] In this work, Hinogami et al. utilized Cu rubenate (CR) MOFs on carbon paper for the selective reduction of CO_2 to formic acid in an aqueous solution of $KHCO_3$ with a 30% current efficiency. Compared with a normal Cu electrode, the CR-MOF was much more efficient and selective during the reduction. This higher selectivity was attributed to the lower electron densities at the metal centers and weaker adsorption of the reactant CO_2 on the MOF surface. Subsequently, MOFs were extensively studied as

catalysts for the synthesis of C_1 products (CH_4, CO, HCOOH and CH_3OH) and C_{2+} products (C_2H_4, EtOH, C_2H_6 and CH_3COOH).[164–167]

Majidi et al. prepared a two-dimensional (2D) Cu-based conductive MOF (Cu tetrahydroxyquinone (Cu–THQ)) having excellent catalytic activity (Fig. 10).[164] In this material, reduced Cu (Cu^+) was reversibly converted to Cu^{2+} after the CO_2RR reaction. Cu–THQ nanoflakes with an average lateral size of 140 nm exhibited a negligible overpotential of 16 mV for activation, a high current density of approximately 173 mA cm^{-2} at -0.45 V vs. RHE, an average FE of approximately 91% for CO production and a remarkable TOF as high as approximately 20.82 s^{-1}. Yang et al. synthesized a so-called Cu-ade MOF comprising Cu^{2+} ions coordinated with adeninato/carboxylato ligands and employed this material to promote electrocatalytic CO_2 conversion to C_2H_4. A maximum FE of 45.0% was achieved at -1.4 V vs. RHE in a CO_2-purged 0.1 mol L^{-1} $KHCO_3$ electrolyte.[165] Recently, Wang et al. reported a novel CO_2RR catalyst consisting of CuO nanoparticles with sizes ranging from 1.4 to 3.3 nm anchored on Cu-MOF nanosheets that was obtained through a one-step facile solvothermal method. The electrocatalytic performance was significantly promoted by the interface between the CuO and Cu-MOF and the accessible metallic moieties and unique 2D structure of the Cu-MOF enhanced the adsorption and activation of CO_2 molecules.[166] Notably, compared with state-of-the-art 2D PcCu–Cu–O, the overpotential required to obtain a similar FE for C_2H_4 formation (50.0%) over the CuO/Cu-MOF composite was substantially lowered by 100 mV.[168] Liu et al. prepared a 2D conductive MOF using a nitrogen-rich tricycloquinazoline (TQ)-based multitopic catechol ligand to coordinate Cu^{2+} and Ni^{2+} ions and form 2D graphene-like porous sheets ($M_3(HHTQ)_2$) (M = Cu, Ni; HHTQ = 2,3,7,8, 12,13-hexahydroxytricycloquinazoline).[169] A $Cu_3(HHTQ)_2$ specimen exhibited superior catalytic activity during the CO_2RR with CH_3OH as the sole product and an FE of 53.6% at a small overpotential of -0.4 V.

Carbonization and oxidation of Cu based MOF also have been proved to be an effective approach to improve the activity and selectivity of CO_2RR, which can achieve high current density due to the presence of carbon matrix in addition to the intrinsic characteristics of MOFs remaining.[170–172] Liang et al. prepared Cu-based catalyst derived from Cu-MOF, which remained porous morphology of Cu-MOF and achieved the conversion of CO2 to C_{2+} products.[172] The optimized catalyst exhibits a 51% FE for C_2H_4 and a 70% FE for C_{2+} products, with 20 h operational stability in an H-cell configuration, and a partial ethylene current density of 150 mA cm^{-2} in a flow-cell configuration. The formation of bimetallic catalysts could change the electronic structure, and decrease the energy barriers for CO_2 activation. Yang et al. synthesized rod-like CuBi bimetallic catalysts by carbonization and oxidation of CuBi-MOF precursors, showing an allured high FE formate of 100% at -0.77 V and excellent durability.[170] The Bi_2CuO_4 in the interface of catalyst greatly enhanced the activity and selectivity of the bimetallic CuBi catalysts. Recently, Xue et al. prepared a Cu/Bi bi-metal catalyst derived from MOFs by a hydrothermal
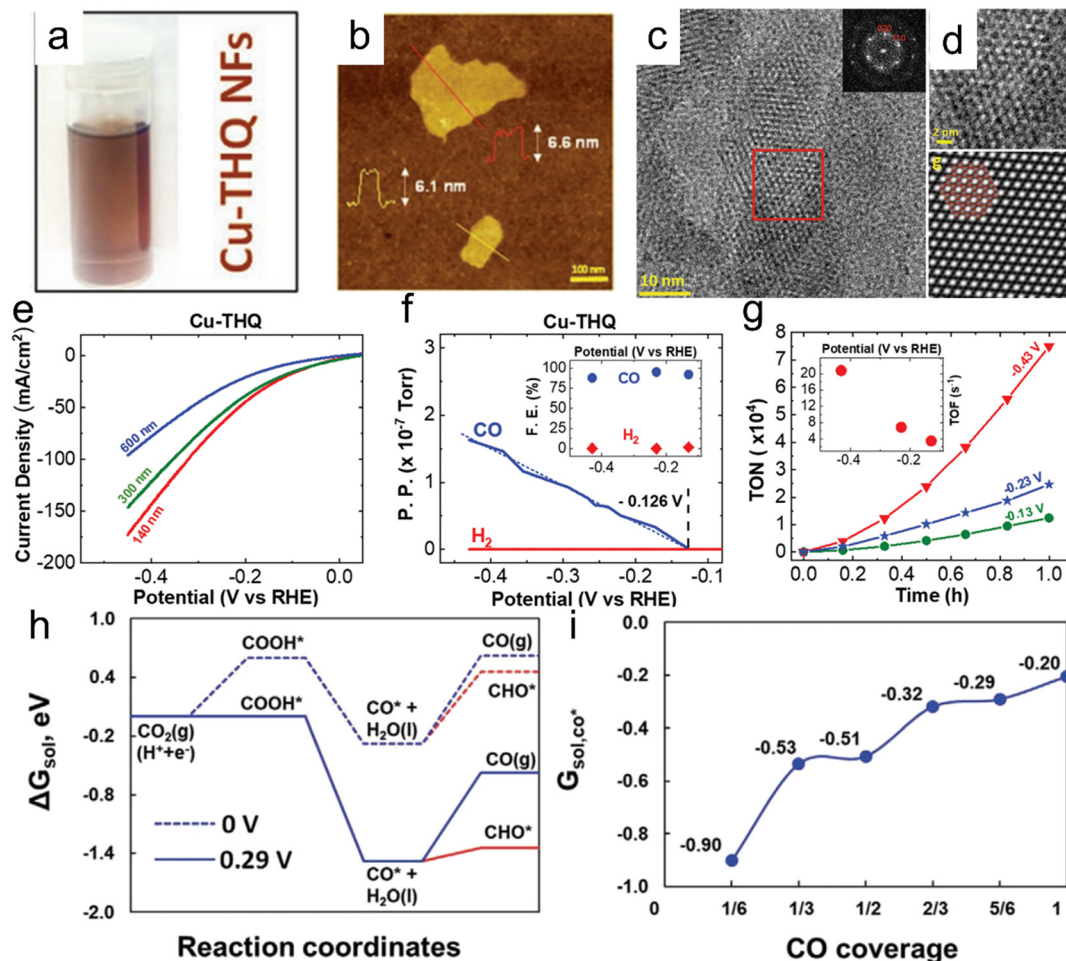
Fig. 10 (a) Cu–THQ NFs dispersed in IPA, (b) a representative AFM image of Cu–THQ NFs, (c) HRTEM images of Cu–THQ NFs along the [001] direction showing elliptical pore packing, (d) an enlarged view of the HRTEM image in the red box shown in panel (c) and corresponding lattice-averaged and symmetry-imposed image, (e) LSV results obtained during the CO$_2$RR in a solution of 1 M choline chloride and 1 M KOH using Cu–THQ NFs having different particle sizes, (f) DEMS analysis results for CO and H$_2$ production during an LSV experiment with Cu–THQ NFs, (g) TON values for CO production during 1 h chronoamperometry experiments at controlled potentials (the inset shows TOFs at these potentials after 1 h), (h) free energies including solvation corrections for CO production on Cu–THQ at 0 V *vs.* RHE (dotted blue lines) and at an overpotential, η, of 0.29 V (solid blue lines) and (i) adsorption free energies of CO at different coverages on Cu–THQ. Reproduction with permission from ref. 164, Copyright 2021, Wiley-VCH.

synthesis combining with calcination under N$_2$ atmosphere, which shows cylindrical morphology composed of bi-metallic nanoparticles.[171] The Cu/Bi bi-metallic system lowered the activate energy barrier of CO$_2$ and shows a strong adsorption capability for the CO$_2$–intermediate. The optimized Cu$_1$–Bi/Bi$_2$O$_3$@C exhibits excellent selectivity toward HCOOH with FE of 93% at −0.94 V.

4. Conclusion and perspectives

This review introduced standard criteria used to evaluate the performance of CO$_2$RR systems and assessed recent advances in the innovation and development of Cu-based CO$_2$RR electrocatalysts. These materials have included monometallic Cu, Cu-based oxides and other Cu-based compounds, Cu-based bimetallics, single/dual Cu atoms and Cu-based MOFs. The

results of prior studies and the performance data for various electrocatalysts were summarized in Table 1. It was noted that certain electrocatalysts have shown excellent catalytic activity and selectivity as well as suitable levels of stability during the CO$_2$RR. Although much has been achieved in this regard, many challenges remain to be overcome and many areas must still be explored. The following are some of the most important advancements, challenges and potential research associated with this field of study.

(1) CO$_2$RR performance should be improved by controlling various reaction conditions, such as the electrolyte that is used, as well as by modification of the Cu catalyst surface and the application of an external electric field or electric–thermal coupling. CO$_2$ conversion to value-added C$_{2+}$ chemicals could be enhanced with the aid of localized electric-thermal field synergy as a means of improving the activity and selectivity of the CO$_2$RR.[173]

Table 1 A summary of reported performance data for Cu-based CO_2RR electrocatalysts

Catalyst	Products	Electrolyte	Performance	Ref.
$Cu(OH)_2$-D/Cu	C_{2+}	CO_2-Saturated 0.1 M $NaHCO_3$	FEs of $\sim$58% for C_2H_4 and $\sim$87% for C_{2+} hydrocarbons and alcohols with the C_{2+} partial current density of $\sim$217 mA cm^{-2} only at -0.54 V	82
(100)-Rich Cu	C_2H_4, CH_3COO, C_2H_5OH, n-C_3H_7OH	CO_2-Saturated 0.1 M $NaHCO_3$	C_{2+} FEs of 88% and partial current density of 320 mA cm^{-2} at -0.63 V	81
Activated Cu nanowires	C_2H_4	CO_2-Saturated 0.1 M $KHCO_3$	C_2H_4 FEs of $\sim$77% at -1.01 ± 0.01 V	84
OD-Cu-500	CO, $HCOO^-$	CO_2-Saturated 0.1 M $NaHCO_3$	CO and $HCOO^-$ FEs of $\sim$45% at -0.3 V	87
Cu nanowires	CO	CO_2-Saturated 0.1 M $NaHCO_3$	CO FEs of $\sim$60% and current density of 1 mA cm^{-2} at an overpotential of 0.3 V	90
Star decahedron Cu NPs	C_2H_4	CO_2-Saturated 0.1 M $KHCO_3$	C_2H_4 FEs of 52.43% at -0.993 V	94
Cu nanosheets with nano-scaled defects	C_2H_4	CO_2-Saturated 0.1 M K_2SO_4	C_2H_4 FEs of 83.2% at -1.2 V	95
Defect-site-rich Cu catalyst	C_{2+} alcohols	CO_2-Saturated 0.1 M $KHCO_3$	C_{2+} alcohols FEs of 70%	96
Cu nanoneedle arrays	C_{2+}	CO_2-Saturated 0.1 M $KHCO_3$	C_{2+} FEs of 59% at -1.2 V (*vs.* RHE)	97
Electron beam (EB) Cu catalyst	C_2H_4	15 sccm CO_2 and 1 M KOH	C_2H_4 FEs of 39% and C_{2+} FE of 70% at -0.65 V *vs.* RHE	98
Ditetrahedron-shaped Cu_8	HCOOH	CO_2-Saturated 0.5 M $KHCO_3$	HCOOH FE of $\sim$92% at -1.0 V *vs.* RHE	101
Amorphous Cu NPs	HCOOH, C_2H_6O	CO_2-Saturated 0.1 M $KHCO_3$	C_2 FE of 59% at -1.4 V with formic acid (HCOOH) and ethanol (C_2H_6O) account for 37% and 22%.	103
CV-treated Cu electrode	C_2H_4	CO_2-Saturated 0.1 M $KHCO_3$	C_2H_4 FE of 40% at -1 V *versus* RHE	111
Anodic treated Cu	C_{2+}	CO_2-Saturated 0.1 M $KHCO_3$	C_{2+} FE of 76% at -1.0 V *versus* RHE.	112
Cu oxide with surface oxygen vacancies	C_2H_4	CO_2-Saturated 0.1 M $KHCO_3$	C_2H_4 FE of $\sim$63% at -1.4 *versus* RHE	113
Cu_2O-BN	CO, C_2H_4	CO_2-Saturated 0.5 M $KHCO_3$	CO FE of $\sim$14% at -1.2 V *versus* RHE, C_2H_4 FE of $\sim$16% at -1.4 V *versus* RHE	118
Cu_2S	Formate	CO_2-Saturated 0.1 M $NaHCO_3$ aqueous solution	Formate FE of 87% and partial current density over 19 mA cm^{-2} at -0.9 V *vs.* RHE	121
Cu_2S–Cu–V NPs	C_3H_7OH, C_2H_5OH	CO_2-Saturated 0.1 M $KHCO_3$ aqueous solution	FE for C_3H_7OH and C_2H_5OH reaches 8 ± 0.7% and 15 ± 1% with a partial current density of 2.5 ± 0.1 and 4.8 ± 0.1 mA cm^{-2} at -0.95 V *vs.* RHE	122
CuS with double sulfur vacancies	n-Propanol	CO_2-Saturated 0.1 M $KHCO_3$ aqueous solution	n-Propanol FE of 15.4 ± 1% at -1.05 V *vs.* RHE	63
CuS	HCOOH	CO_2-Saturated 0.1 M $KHCO_3$ aqueous solution	HCOOH FE of $\sim$60%	123
CuS	CH_4	CO_2-Saturated 0.1 M $KHCO_3$ aqueous solution	CH_4 FE of $\sim$73%	124
$Cu_{2-x}Se$	Methanol	CO_2-Saturated [Bmim]PF_6-CH_3CN-H_2O	Methanol FE of 77.6% and current density of 41.5 mA cm^{-2} at a low overpotential of 285 mV	126
Se-defective $CuInSe_2$	CO	CO_2-Saturated 0.5 M $KHCO_3$ aqueous solution	CO FE of 91% at -0.7 V *vs.* RHE	127
Cu_3P NS/Cu	Formate	CO_2-Saturated 0.1 M $KHCO_3$	FE of 90% at a low overpotential of 65 mV	125
Cu_3N	C_{2+}	1 M KOH	FE of 73.7% under -1100 mA cm^{-2}, C_{2+} partial current density of -909 mA cm^{-2} at -1.15 V *vs.* RHE	128
CuPd	CO, C_2	CO_2-Saturated 0.1 M $KHCO_3$ aqueous solution	The ordered CuPd exhibits the highest CO FE of $\sim$80% The separated CuPd exhibits the highest FE (up to 63%) for C_2 such as C_2H_4 and C_2H_5OH	130
$Cu_{100-x}Co_x$ NPs	HCOOH and CO	CO_2-Saturated 0.1 M $KHCO_3$ aqueous solution	$Cu_{90}Co_{10}$ at constant NP size of $\sim$5.2 nm show HCOOH FE of $\sim$10% and CO FE of 7% at -1.1 *vs.* RHE	132
CuZn NPs	CO, CH_4	CO_2-Saturated 0.1 M $KHCO_3$ aqueous solution	CH_4 FE of $\sim$70% (Zn contents from 10–50), CO FE of $\sim$40% (Zn contents from 70–100)	133
Cu–Ag Tandem catalysts	C_2H_4, C_2H_5OH, CH_3COO^-	1 M KOH	C_{2+} partial current over a Cu surface increases from 37 to 160 mA cm^{-2} At 0.70 V *vs.* RHE	135
Gold NPs on Cu foil	Ethanol and n-propanol	CO_2-Saturated 0.1 M $KHCO_3$ aqueous solution	Alcohol production is observed at over 265 mV more positive potentials on the Au/Cu catalyst compared with Cu	137
$In_{1.5}Cu_{0.5}$ NPs	HCOOH	CO_2-Saturated 0.1 M $KHCO_3$ aqueous solution	HCOOH FE of 90% at -1.2 V *vs.* RHE	141
Cu–CuI composite catalyst	C_{2+}	1 M KOH	C_{2+} partial current density of 591 mA cm^{-2} at -1.0 V *vs.* RHE	142
Cu_2Sb decorated Cu nanowire arrays	CO	CO_2-Saturated 0.1 M $KHCO_3$ aqueous solution	CO FE of 86.5% at -0.90 V *vs.* RHE	143
Cu–Sn bimetallic catalyst	CO	CO_2-Saturated 0.1 M $KHCO_3$ aqueous solution	CO FE of 90% and a current density of -1.0 mA cm^{-2} at -0.6 V *vs.* RHE	144
Porous Cu6.26Sn5	Formate	CO_2-Saturated 0.1 M $KHCO_3$ aqueous solution	Formate FE of 97.8 ± 2.4% at -1.08 V *vs.* RHE	145
	CH_3OH, CO	CO_2-Saturated 0.1 M $KHCO_3$ aqueous solution	FE of 44% for CH_3OH and 56% for CO at the potentials of 0.9 *vs.* RHE	150

Table 1 (continued)

Catalyst	Products	Electrolyte	Performance	Ref.
Cu–SACs/TCNFs (through-hole carbon nanofibers)				
Cu–SACs/nitrogen-doped carbon	CH_4, C_2H_4	CO_2-Saturated 0.1 M $KHCO_3$ aqueous solution	Cu–N_2 with C_2H_4 FE of 24.8% at 1.4 V, Cu–N_4 with CH_4 FE of 38.6% at 1.6 V.	7
Cu–SA/NPC	CH_3COCH_3	CO_2-Saturated electrolyte	FE of 36.7% and production rate of 336.1 μg h^{-1} at 0.36 V.	151
Carbon-dots-based SAC with unique CuN_2O_2 sites	CH_4	CO_2-Saturated 0.5 M $KHCO_3$ solution	CH_4 FE of 78% and selectivity of 99% with current density of 40 mA cm^{-2} at 1.64 V.	152
Cu–C_3N_4	C_2H_5OH, C_2H_4, and C_2H_6	0.1 M $KHCO_3$ solution	—	156
Cu–CeO_2-4% nanorods	CH_4	CO_2-Saturated 0.1 M $KHCO_3$ aqueous solution	CH_4 FE of $\sim$58% at −1.8 V vs. RHE	153
Cu/p-Al_2O_3 SAC	CH_4	—	CH_4 FE of 62% at −1.2 V with current density of 153.0 mA cm^{-2}.	157
Cu SA/MXene	CH_3OH	CO_2-Saturated in the electrolyte	CH_3OH FE of 59.1%	155
Ni–Cu dual atom catalysts	CO	CO_2-Saturated 0.5 M $KHCO_3$ solution	TOF of 20 695 h^{-1} and CO FE of 97.7% at −0.6 V	160
HKUST-1	CH_3OH, CH_3CH_2OH	CO_2-Saturated 0.5 M KHCO3	Methanol FE of 5.6% and ethanol FE of 10.3% at −1.0 vs. Ag/AgCl	175
Cu/C	CH_3OH, CH_3CH_2OH	CO_2-Saturated 0.1 M $KHCO_3$	Methanol FE of 43.2%, ethanol FE of 34.8% at −0.1 V vs. RHE	176
Cu/Bi-MOFs	CH_3OH, CH_3CH_2OH	CO_2-Saturated 0.5 M $KHCO_3$	Methanol FE of 18.2%, ethanol FE of 28.3% at −0.37 vs. RHE	177
CuPc	CH_4	CO_2-Saturated 0.5 M $KHCO_3$	CH_4 FE of 66% at −1.06 vs. RHE	178
Cu-MOF-74/Cu NPs	CH_4	CO_2-Saturated 0.1 M $KHCO_3$	CH_4 FE of >50% at −1.3 vs. RHE	179

(2) Compared with that of other transition metals, the selectivity of Cu-based nanomaterials for specific CO_2RR products is very low. Optimization of these materials is therefore required, particularly in the case of the newly-developed Cu-based amorphous and high entropy alloys.

(3) Single/dual atom Cu catalysts can promote the CO_2RR to form different products. Effective approaches to improving the overall selectivity for deep reduction products are necessary, such as the rational design of the structure of single-atom Cu sites and the construction of atom pairs. Other techniques have included the selection of substrate materials having high surface areas and strong coordination sites. Remaining challenges include difficulties in precisely controlling multiple active centers, low intrinsic activities of catalysts, poor loading capacities and low yields of C_{2+} products (the majority of SACs provide CO or HCOOH as the major CO_2RR product). The reversible transformation of Cu-SACs to Cu clusters during the CO_2 reduction process has been established based on operando XAS analyses.[174] Therefore, strategies to improve the stability of Cu-SACs must be devised.

(4) In the case of Cu-based MOFs, the effects of various substituents on organic ligands and metal centers on the CO_2RR activities of these materials should be further investigated. Other potential improvements include the design of conducive ligand structures to facilitate electron transfer and the use of nano-sized 2D structures and bimetallic catalysts to further improve the selectivity and efficiency of CO_2 conversion.

(5) A thorough understanding of changes in the catalyst and of reaction intermediates would be helpful to the rational design of more effective Cu-based CO_2RR catalysts. Such work will require an improved understanding of the CO_2RR mechanism based on a combination of in situ/operando characterization techniques such as in situ spectroscopy and TEM with theoretical calculations.

Conflicts of interest

There are no conflicts to declare.

Acknowledgements

References

1 J. Shi, Y. Jiang, Z. Jiang, X. Wang, X. Wang, S. Zhang, P. Han and C. Yang, Chem. Soc. Rev., 2015, 44, 5981–6000.

2 C. Xiao and J. Zhang, ACS Nano, 2021, 15, 7975–8000.

3 V. A. Semenov, Nat. Climate Change, 2012, 2, 315–316.

4 Q. Schiermeier, Nature, 2011, 470, 316.

5 K. Xiang, F. Shen, Y. Fu, L. Wu, Z. Wang, H. Yi, X. Liu, P. Wang, M. Liu, Z. Lin and H. Liu, Environ. Sci.: Nano, 2022, 9, 911–953.

6 S. Chu, Y. Cui and N. Liu, Nat. Mater., 2016, 16, 16–22.

7 A. Guan, Z. Chen, Y. Quan, C. Peng, Z. Wang, T.-K. Sham, C. Yang, Y. Ji, L. Qian, X. Xu and G. Zheng, ACS Energy Lett., 2020, 5, 1044–1053.

8 G. Singh, J. Lee, A. Karakoti, R. Bahadur, J. Yi, D. Zhao, K. AlBahily and A. Vinu, Chem. Soc. Rev., 2020, 49, 4360–4404.

9 L. Ye, Y. Ying, D. Sun, Z. Zhang, L. Fei, Z. Wen, J. Qiao and H. Huang, Angew. Chem., Int. Ed., 2020, 59, 3244–3251.

10 C. Liu, J. Gong, Z. Gao, L. Xiao, G. Wang, J. Lu and L. Zhuang, *Sci. China: Chem.*, 2021, **64**, 1660–1678.

11 P. De Luna, C. Hahn, D. Higgins, S. A. Jaffer, T. F. Jaramillo and E. H. Sargent, *Science*, 2019, **364**, eaav3506.

12 E. B. Creel and B. D. McCloskey, *Nat. Catal.*, 2018, **1**, 6–7.

13 F. Li, D. R. MacFarlane and J. Zhang, *Nanoscale*, 2018, **10**, 6235–6260.

14 M. M. Ayyub and C. N. R. Rao, *Mater. Horiz.*, 2021, **8**, 2420–2443.

15 Y. Hori, K. Kikuchi and S. Suzuki, *Chem. Lett.*, 1985, 1695–1698.

16 Y. Du, X. Meng, Z. Wang, X. Zhao and J. Qiu, *Acta Phys. Chim. Sin.*, 2021, **0**, 2101009.

17 J. Chen, T. Wang, Z. Li, B. Yang, Q. Zhang, L. Lei, P. Feng and Y. Hou, *Nano Res.*, 2021, **14**, 3188–3207.

18 S. Nitopi, E. Bertheussen, S. B. Scott, X. Liu, A. K. Engstfeld, S. Horch, B. Seger, I. E. L. Stephens, K. Chan, C. Hahn, J. K. Norskov, T. F. Jaramillo and I. Chorkendorff, *Chem. Rev.*, 2019, **119**, 7610–7672.

19 Q. Zhu, J. Ma, X. Kang, X. Sun, H. Liu, J. Hu, Z. Liu and B. Han, *Angew. Chem., Int. Ed.*, 2016, **55**, 9012–9016.

20 W. Zhu, Y. J. Zhang, H. Zhang, H. Lv, Q. Li, R. Michalsky, A. A. Peterson and S. Sun, *J. Am. Chem. Soc.*, 2014, **136**, 16132–16135.

21 H. Yang, N. Han, J. Deng, J. Wu, Y. Wang, Y. Hu, P. Ding, Y. Li, Y. Li and J. Lu, *Adv. Energy Mater.*, 2018, **8**(35), 1801536.

22 C. Zhang, S. Yang, J. Wu, M. Liu, S. Yazdi, M. Ren, J. Sha, J. Zhong, K. Nie, A. S. Jalilov, Z. Li, H. Li, B. I. Yakobson, Q. Wu, E. Ringe, H. Xu, P. M. Ajayan and J. M. Tour, *Adv. Energy Mater.*, 2018, **8**(19), 1703487.

23 H. Chen, J. Chen, J. Si, Y. Hou, Q. Zheng, B. Yang, Z. Li, L. Gao, L. Lei, Z. Wen and X. Feng, *Chem. Sci.*, 2020, **11**, 3952–3958.

24 Y. Fu, T. Wang, W. Zheng, C. Lei, B. Yang, J. Chen, Z. Li, L. Lei, C. Yuan and Y. Hou, *ACS Appl. Mater. Interfaces*, 2020, **12**, 16178–16185.

25 F. Wei, T. Wang, X. Jiang, Y. Ai, A. Cui, J. Cui, J. Fu, J. Cheng, L. Lei, Y. Hou and S. Liu, *Adv. Funct. Mater.*, 2020, **30**(39), 2002092.

26 H. Shang, T. Wang, J. Pei, Z. Jiang, D. Zhou, Y. Wang, H. Li, J. Dong, Z. Zhuang, W. Chen, D. Wang, J. Zhang and Y. Li, *Angew. Chem., Int. Ed.*, 2020, **59**, 22465–22469.

27 W. Zheng, J. Yang, H. Chen, Y. Hou, Q. Wang, M. Gu, F. He, Y. Xia, Z. Xia, Z. Li, B. Yang, L. Lei, C. Yuan, Q. He, M. Qiu and X. Feng, *Adv. Funct. Mater.*, 2020, **30**(4), 1907658.

28 K. P. Kuhl, E. R. Cave, D. N. Abram and T. F. Jaramillo, *Energy Environ. Sci.*, 2012, **5**, 7050–7059.

29 S. Popovic, M. Smiljanic, P. Jovanovic, J. Vavra, R. Buonsanti and N. Hodnik, *Angew. Chem., Int. Ed.*, 2020, **59**, 14736–14746.

30 C. Zhao and J. Wang, *Chem. Eng. J.*, 2016, **293**, 161–170.

31 Y. Wang, X.-P. Zhang, H. Lei, K. Guo, G. Xu, L. Xie, X. Li, W. Zhang, U.-P. Apfel and R. Cao, *CCS Chem.*, 2022, **0**, 1–9.

32 D. M. Weekes, D. A. Salvatore, A. Reyes, A. Huang and C. P. Berlinguette, *Acc. Chem. Res.*, 2018, **51**, 910–918.

33 B. A. Rosen, A. Salehi-Khojin, M. R. Thorson, W. Zhu, D. T. Whipple, P. J. Kenis and R. I. Masel, *Science*, 2011, **334**, 643–644.

34 J. Wu, F. G. Risalvato, P. P. Sharma, P. J. Pellechia, F.-S. Ke and X.-D. Zhou, *J. Electrochem. Soc.*, 2013, **160**, F953–F957.

35 D. T. Whipple, E. C. Finke and P. J. A. Kenis, *Electrochem. Solid-State Lett.*, 2010, **13**, B109.

36 N. S. Spinner, J. A. Vega and W. E. Mustain, *Catal. Sci. Technol.*, 2012, **2**, 19–28.

37 E. L. Clark, M. R. Singh, Y. Kwon and A. T. Bell, *Anal. Chem.*, 2015, **87**, 8013–8020.

38 A. S. Varela, W. Ju, T. Reier and P. Strasser, *ACS Catal.*, 2016, **6**, 2136–2144.

39 C. Zou, C. Xi, D. Wu, J. Mao, M. Liu, H. Liu, C. Dong and X.-W. Du, *Small*, 2019, **15**, 1902582.

40 F. Zhang and A. C. Co, *Angew. Chem., Int. Ed.*, 2020, **59**, 1674–1681.

41 M. R. Singh, Y. Kwon, Y. Lum, J. W. Ager and A. T. Bell, *J. Am. Chem. Soc.*, 2016, **138**, 13006–13012.

42 J. Resasco, L. D. Chen, E. Clark, C. Tsai, C. Hahn, T. F. Jaramillo, K. Chan and A. T. Bell, *J. Am. Chem. Soc.*, 2017, **139**, 11277–11287.

43 S. Ringe, E. L. Clark, J. Resasco, A. Walton, B. Seger, A. T. Bell and K. Chan, *Energy Environ. Sci.*, 2019, **12**, 3001–3014.

44 S. Kaneco, K. Iiba, S.-K. Suzuki, K. Ohta and T. Mizuno, *J. Phys. Chem. B*, 1999, **103**, 7456–7460.

45 N. V. Rees and R. G. Compton, *Energy Environ. Sci.*, 2011, **4**, 403–408.

46 N. Hollingsworth, S. F. R. Taylor, M. T. Galante, J. Jacquemin, C. Longo, K. B. Holt, N. H. de Leeuw and C. Hardacre, *Angew. Chem., Int. Ed.*, 2015, **54**, 14164–14168.

47 V. Vedharathinam, Z. Qi, C. Horwood, B. Bourcier, M. Stadermann, J. Biener and M. Biener, *ACS Catal.*, 2019, **9**, 10605–10611.

48 B. Braunschweig, P. Mukherjee, J. L. Haan and D. D. Dlott, *J. Electroanal. Chem.*, 2017, **800**, 144–150.

49 Z. Han, D. Han, Z. Chen, J. Gao, G. Jiang, X. Wang, S. Lyu, Y. Guo, C. Geng, L. Yin, Z. Weng and Q.-H. Yang, *Nat. Commun.*, 2022, **13**, 3158.

50 A. A. Peterson, F. Abild-Pedersen, F. Studt, J. Rossmeisl and J. K. Nørskov, *Energy Environ. Sci.*, 2010, **3**, 1311–1315.

51 J. T. Feaster, C. Shi, E. R. Cave, T. Hatsukade, D. N. Abram, K. P. Kuhl, C. Hahn, J. K. Nørskov and T. F. Jaramillo, *ACS Catal.*, 2017, **7**, 4822–4827.

52 Y. Hori, A. Murata, R. Takahashi and S. Suzuki, *J. Am. Chem. Soc.*, 1987, **109**, 5022–5023.

53 K. J. P. Schouten, Z. Qin, E. Pérez Gallent and M. T. M. Koper, *J. Am. Chem. Soc.*, 2012, **134**, 9864–9867.

54 W. Luo, X. Nie, M. J. Janik and A. Asthagiri, *ACS Catal.*, 2016, **6**, 219–229.

55 H. Xiao, T. Cheng and W. A. Goddard, 3rd, *J. Am. Chem. Soc.*, 2017, **139**, 130–136.

56 A. J. Garza, A. T. Bell and M. Head-Gordon, *ACS Catal.*, 2018, **8**, 1490–1499.

57 B. Zha, C. Li and J. Li, *J. Catal.*, 2020, **382**, 69–76.

58 Q. Qian, J. Zhang, M. Cui and B. Han, *Nat. Commun.*, 2016, **7**, 11481.

59 X. F. Qiu, J. R. Huang, C. Yu, Z. H. Zhao, H. L. Zhu, Z. Ke, P. Q. Liao and X. M. Chen, *Angew. Chem., Int. Ed.*, 2022, **61**, e202206470.

60 A. D. Handoko, K. W. Chan and B. S. Yeo, *ACS Energy Lett.*, 2017, **2**, 2103–2109.

61 C. Chen, X. Yan, S. Liu, Y. Wu, Q. Wan, X. Sun, Q. Zhu, H. Liu, J. Ma, L. Zheng, H. Wu and B. Han, *Angew. Chem., Int. Ed.*, 2020, **59**, 16459–16464.

62 M.-G. Kim, Y. Choi, E. Park, C.-H. Cheon, N.-K. Kim, B. K. Min and W. Kim, *ACS Appl. Energy Mater.*, 2020, **3**, 11516–11522.

63 C. Peng, G. Luo, J. Zhang, M. Chen, Z. Wang, T.-K. Sham, L. Zhang, Y. Li and G. Zheng, *Nat. Commun.*, 2021, **12**, 1580.

64 C. Liu, T. Wang, D. Hao, Q. Li, S. Li and C. Sun, *J. Mater. Sci. Technol.*, 2022, **110**, 96–102.

65 N. Li, X. Chen, W.-J. Ong, D. R. MacFarlane, X. Zhao, A. K. Cheetham and C. Sun, *ACS Nano*, 2017, **11**, 10825–10833.

66 R. Zhang, Y. Zhang, L. Liu, X. Li, Y. Tang, Y. Ni, C. Sun and H. Zhang, *Appl. Surf. Sci.*, 2022, **582**, 152472.

67 A. A. Peterson and J. K. Nørskov, *J. Phys. Chem. Lett.*, 2012, **3**, 251–258.

68 Y. Ji, J. K. Nørskov and K. Chan, *J. Phys. Chem. C*, 2019, **123**, 4256–4261.

69 C. Shi, H. A. Hansen, A. C. Lausche and J. K. Nørskov, *Phys. Chem. Chem. Phys.*, 2014, **16**, 4720–4727.

70 S. Zheng, C. Zuo, X. Liang, S. Li and F. Pan, *J. Energy Chem.*, 2021, **56**, 444–448.

71 H. Xin, A. Vojvodic, J. Voss, J. K. Nørskov and F. Abild-Pedersen, *Phys. Rev. B: Condens. Matter Mater. Phys.*, 2014, **89**, 115114.

72 C. Ren, S. Lu, Y. Wu, Y. Ouyang, Y. Zhang, Q. Li, C. Ling and J. Wang, *J. Am. Chem. Soc.*, 2022, **144**, 12874–12883.

73 S. Jin, Z. Hao, K. Zhang, Z. Yan and J. Chen, *Angew. Chem., Int. Ed.*, 2021, **60**, 20627–20648.

74 C. Chen, J. F. Khosrowabadi Kotyk and S. W. Sheehan, *Chem*, 2018, **4**, 2571–2586.

75 R. Küngas, P. Blennow, T. Heiredal-Clausen, T. Holt, J. Rass-Hansen, S. Primdahl and J. B. Hansen, *ECS Trans.*, 2017, **78**, 2879–2884.

76 R. Krause, D. Reinisch, C. Reller, H. Eckert, D. Hartmann, D. Taroata, K. Wiesner-Fleischer, A. Bulan, A. Lueken and G. Schmid, *Chem. Ing. Tech.*, 2020, **92**, 53–61.

77 D. Raciti and C. Wang, *ACS Energy Lett.*, 2018, **3**, 1545–1556.

78 K. P. Kuhl, E. R. Cave, D. N. Abram and T. F. Jaramillo, *Energy Environ. Sci.*, 2012, **5**, 7050–7059.

79 Y. Hori, I. Takahashi, O. Koga and N. Hoshi, *J. Mol. Catal. A: Chem.*, 2003, **199**, 39–47.

80 K. Jiang, R. B. Sandberg, A. J. Akey, X. Liu, D. C. Bell, J. K. Nørskov, K. Chan and H. Wang, *Nat. Catal.*, 2018, **1**, 111–119.

81 Y. H. Wang, Z. Y. Wang, C. T. Dinh, J. Li, A. Ozden, M. G. Kibria, A. Seifitokaldani, C. S. Tan, C. M. Gabardo, M. C. Luo, H. Zhou, F. W. Li, Y. Lum, C. McCallum, Y. Xu, M. X. Liu, A. Proppe, A. Johnston, P. Todorovic, T. T. Zhuang, D. Sinton, S. O. Kelley and E. H. Sargent, *Nat. Catal.*, 2020, **3**, 98–106.

82 D. Zhong, Z. J. Zhao, Q. Zhao, D. Cheng, B. Liu, G. Zhang, W. Deng, H. Dong, L. Zhang, J. Li, J. Li and J. Gong, *Angew. Chem., Int. Ed.*, 2021, **60**, 4879–4885.

83 A. Bagger, W. Ju, A. S. Varela, P. Strasser and J. Rossmeisl, *ACS Catal.*, 2019, **9**, 7894–7899.

84 C. Choi, S. Kwon, T. Cheng, M. Xu, P. Tieu, C. Lee, J. Cai, H. M. Lee, X. Pan, X. Duan, W. A. Goddard and Y. Huang, *Nat. Catal.*, 2020, **3**, 804–812.

85 L. Zaza, K. Rossi and R. Buonsanti, *ACS Energy Lett.*, 2022, **7**, 1284–1291.

86 M. Song, Z. Jiao, W. Jing, Y. Liu and L. Guo, *J. Phys. Chem. Lett.*, 2022, **13**, 4434–4440.

87 C. W. Li and M. W. Kanan, *J. Am. Chem. Soc.*, 2012, **134**, 7231–7234.

88 C. W. Li, J. Ciston and M. W. Kanan, *Nature*, 2014, **508**, 504–507.

89 A. Verdaguer-Casadevall, C. W. Li, T. P. Johansson, S. B. Scott, J. T. McKeown, M. Kumar, I. E. L. Stephens, M. W. Kanan and I. Chorkendorff, *J. Am. Chem. Soc.*, 2015, **137**, 9808–9811.

90 D. Raciti, K. J. Livi and C. Wang, *Nano Lett.*, 2015, **15**, 6829–6835.

91 L. Cao, D. Raciti, C. Li, K. J. T. Livi, P. F. Rottmann, K. J. Hemker, T. Mueller and C. Wang, *ACS Catal.*, 2017, **7**, 8578–8587.

92 D. Cheng, Z. J. Zhao, G. Zhang, P. Yang, L. Li, H. Gao, S. Liu, X. Chang, S. Chen, T. Wang, G. A. Ozin, Z. Liu and J. Gong, *Nat. Commun.*, 2021, **12**, 395.

93 T. Luo, K. Liu, J. Fu, S. Chen, H. Li, J. Hu and M. Liu, *J. Energy Chem.*, 2022, **70**, 219–223.

94 C. Choi, T. Cheng, M. Flores Espinosa, H. Fei, X. Duan, W. A. Goddard III and Y. Huang, *Adv. Mater.*, 2019, **31**, 1805405.

95 B. Zhang, J. Zhang, M. Hua, Q. Wan, Z. Su, X. Tan, L. Liu, F. Zhang, G. Chen, D. Tan, X. Cheng, B. Han, L. Zheng and G. Mo, *J. Am. Chem. Soc.*, 2020, **142**, 13606–13613.

96 Z. Gu, H. Shen, Z. Chen, Y. Yang, C. Yang, Y. Ji, Y. Wang, C. Zhu, J. Liu, J. Li, T.-K. Sham, X. Xu and G. Zheng, *Joule*, 2021, **5**, 429–440.

97 Y. Zhou, Y. Liang, J. Fu, K. Liu, Q. Chen, X. Wang, H. Li, L. Zhu, J. Hu, H. Pan, M. Miyauchi, L. Jiang, E. Cortés and M. Liu, *Nano Lett.*, 2022, **22**, 1963–1970.

98 E. Jeng, Z. Qi, A. R. Kashi, S. Hunegnaw, Z. Huo, J. S. Miller, L. B. Bayu Aji, B. H. Ko, H. Shin, S. Ma, K. P. Kuhl, F. Jiao and J. Biener, *ACS Appl. Mater. Interfaces*, 2022, **14**, 7731–7740.

99 H. Dong, Y. Li and D.-E. Jiang, *J. Phys. Chem. C*, 2018, **122**, 11392–11398.

100 S. Zhang, L. Chen, X. S. Luan and H. Li, *Chem. Phys.*, 2022, **557**, 111487.

101 L. J. Liu, Z. Y. Wang, Z. Y. Wang, R. Wang, S. Q. Zang and T. C. W. Mak, *Angew. Chem., Int. Ed.*, 2022, **134**(35), e202205626.

102 S. J. Li, D. Bao, M. M. Shi, B. R. Wulan, J. M. Yan and Q. Jiang, *Adv. Mater.*, 2017, **29**(33), 1700001.

103 Y.-X. Duan, F.-L. Meng, K.-H. Liu, S.-S. Yi, S.-J. Li, J.-M. Yan and Q. Jiang, *Adv. Mater.*, 2018, **30**, 1706194.

104 Z.-Z. Wu, F.-Y. Gao and M.-R. Gao, *Energy Environ. Sci.*, 2021, **14**, 1121–1139.

105 H. Xiao, W. A. Goddard, T. Cheng and Y. Liu, *Proc. Natl. Acad. Sci.*, 2017, **114**, 6685–6688.

106 Y. Zhou, F. Che, M. Liu, C. Zou, Z. Liang, P. De Luna, H. Yuan, J. Li, Z. Wang, H. Xie, H. Li, P. Chen, E. Bladt, R. Quintero-Bermudez, T.-K. Sham, S. Bals, J. Hofkens, D. Sinton, G. Chen and E. H. Sargent, *Nat. Chem.*, 2018, **10**, 974–980.

107 P. De Luna, R. Quintero-Bermudez, C.-T. Dinh, M. B. Ross, O. S. Bushuyev, P. Todorović, T. Regier, S. O. Kelley, P. Yang and E. H. Sargent, *Nat. Catal.*, 2018, **1**, 103–110.

108 W. Zhang, C. Huang, Q. Xiao, L. Yu, L. Shuai, P. An, J. Zhang, M. Qiu, Z. Ren and Y. Yu, *J. Am. Chem. Soc.*, 2020, **142**, 11417–11427.

109 Y. Kwon, Y. Lum, E. L. Clark, J. W. Ager and A. T. Bell, *ChemElectroChem*, 2016, **3**, 1012–1019.

110 H. Mistry, A. S. Varela, C. S. Bonifacio, I. Zegkinoglou, I. Sinev, Y.-W. Choi, K. Kisslinger, E. A. Stach, J. C. Yang, P. Strasser and B. R. Cuenya, *Nat. Commun.*, 2016, **7**, 12123.

111 T.-C. Chou, C.-C. Chang, H.-L. Yu, W.-Y. Yu, C.-L. Dong, J.-J. Velasco-Vélez, C.-H. Chuang, L.-C. Chen, J.-F. Lee, J.-M. Chen and H.-L. Wu, *J. Am. Chem. Soc.*, 2020, **142**, 2857–2867.

112 R. M. Arán-Ais, F. Scholten, S. Kunze, R. Rizo and B. Roldan Cuenya, *Nat. Energy*, 2020, **5**, 317–325.

113 Z. X. Gu, N. Yang, P. Han, M. Kuang, B. B. Mei, Z. Jiang, J. Zhong, L. Li and G. F. Zheng, *Small Methods*, 2019, **3**, 1800449.

114 X. Wang, K. Klingan, M. Klingenhof, T. Moller, J. Ferreira de Araujo, I. Martens, A. Bagger, S. Jiang, J. Rossmeisl, H. Dau and P. Strasser, *Nat. Commun.*, 2021, **12**, 794.

115 S. H. Lee, J. C. Lin, M. Farmand, A. T. Landers, J. T. Feaster, J. E. Aviles Acosta, J. W. Beeman, Y. Ye, J. Yano, A. Mehta, R. C. Davis, T. F. Jaramillo, C. Hahn and W. S. Drisdell, *J. Am. Chem. Soc.*, 2021, **143**, 588–592.

116 S. Mu, H. Lu, Q. Wu, L. Li, R. Zhao, C. Long and C. Cui, *Nat. Commun.*, 2022, **13**, 3694.

117 J. Li, A. Ozden, M. Y. Wan, Y. F. Hu, F. W. Li, Y. H. Wang, R. R. Zamani, D. Ren, Z. Y. Wang, Y. Xu, D. H. Nam, J. Wicks, B. Chen, X. Wang, M. C. Luo, M. Graetzel, F. L. Che, E. H. Sargent and D. Sinton, *Nat. Commun.*, 2021, **12**, 2808.

118 Y. Zhou, Y. Yao, R. Zhao, X. Wang, Z. Fu, D. Wang, H. Wang, L. Zhao, W. Ni, Z. Yang and Y.-M. Yan, *Angew. Chem., Int. Ed.*, 2022, e202205832.

119 N. Sakamoto, Y. F. Nishimura, T. Nonaka, M. Ohashi, N. Ishida, K. Kitazumi, Y. Kato, K. Sekizawa, T. Morikawa and T. Arai, *ACS Catal.*, 2020, **10**, 10412–10419.

120 Z. Sun, Y. Hu, D. Zhou, M. Sun, S. Wang and W. Chen, *ACS Energy Lett.*, 2021, **6**, 3992–4022.

121 W. He, I. Liberman, I. Rozenberg, R. Ifraemov and I. Hod, *Angew. Chem., Int. Ed.*, 2020, **59**, 8262–8269.

122 T.-T. Zhuang, Z.-Q. Liang, A. Seifitokaldani, Y. Li, P. De Luna, T. Burdyny, F. Che, F. Meng, Y. Min, R. Quintero-Bermudez, C. T. Dinh, Y. Pang, M. Zhong, B. Zhang, J. Li, P.-N. Chen, X.-L. Zheng, H. Liang, W.-N. Ge, B.-J. Ye, D. Sinton, S.-H. Yu and E. H. Sargent, *Nat. Catal.*, 2018, **1**, 421–428.

123 K. R. Phillips, Y. Katayama, J. Hwang and Y. Shao-Horn, *J. Phys. Chem. Lett.*, 2018, **9**, 4407–4412.

124 Z. Zhao, X. Peng, X. Liu, X. Sun, J. Shi, L. Han, G. Li and J. Luo, *J. Mater. Chem. A*, 2017, **5**, 20239–20243.

125 A. B. Laursen, K. U. D. Calvinho, T. A. Goetjen, K. M. K. Yap, S. Hwang, H. Yang, E. Garfunkel and G. C. Dismukes, *Electrochim. Acta*, 2021, **391**, 138889.

126 D. Yang, Q. Zhu, C. Chen, H. Liu, Z. Liu, Z. Zhao, X. Zhang, S. Liu and B. Han, *Nat. Commun.*, 2019, **10**, 677.

127 J. Wang, X. Zheng, G. Wang, Y. Cao, W. Ding, J. Zhang, H. Wu, J. Ding, H. Hu, X. Han, T. Ma, Y. Deng and W. Hu, *Adv. Mater.*, 2022, **34**, 2106354.

128 M. Zheng, P. Wang, X. Zhi, K. Yang, Y. Jiao, J. Duan, Y. Zheng and S. Z. Qiao, *J. Am. Chem. Soc.*, 2022, **144**, 14936–14944.

129 A. Herzog, A. Bergmann, H. S. Jeon, J. Timoshenko, S. Kuhl, C. Rettenmaier, M. Lopez Luna, F. T. Haase and B. Roldan Cuenya, *Angew. Chem., Int. Ed.*, 2021, **60**, 7426–7435.

130 S. Ma, M. Sadakiyo, M. Heima, R. Luo, R. T. Haasch, J. I. Gold, M. Yamauchi and P. J. A. Kenis, *J. Am. Chem. Soc.*, 2017, **139**, 47–50.

131 D. Kim, J. Resasco, Y. Yu, A. M. Asiri and P. Yang, *Nat. Commun.*, 2014, **5**, 4948.

132 M. Bernal, A. Bagger, F. Scholten, I. Sinev, A. Bergmann, M. Ahmadi, J. Rossmeisl and B. R. Cuenya, *Nano Energy*, 2018, **53**, 27–36.

133 H. S. Jeon, J. Timoshenko, F. Scholten, I. Sinev, A. Herzog, F. T. Haase and B. Roldan Cuenya, *J. Am. Chem. Soc.*, 2019, **141**, 19879–19887.

134 D. Higgins, A. T. Landers, Y. Ji, S. Nitopi, C. G. Morales-Guio, L. Wang, K. Chan, C. Hahn and T. F. Jaramillo, *ACS Energy Lett.*, 2018, **3**, 2947–2955.

135 C. Chen, Y. Li, S. Yu, S. Louisia, J. Jin, M. Li, M. B. Ross and P. Yang, *Joule*, 2020, **4**, 1688–1699.

136 Y. Xu, C. Li, Y. Xiao, C. Wu, Y. Li, Y. Li, J. Han, Q. Liu and J. He, *ACS Appl. Mater. Interfaces*, 2022, **14**, 11567–11574.

137 C. G. Morales-Guio, E. R. Cave, S. A. Nitopi, J. T. Feaster, L. Wang, K. P. Kuhl, A. Jackson, N. C. Johnson, D. N. Abram, T. Hatsukade, C. Hahn and T. F. Jaramillo, *Nat. Catal.*, 2018, **1**, 764–771.

138 W. Luo, W. Xie, M. Li, J. Zhang and A. Züttel, *J. Mater. Chem. A*, 2019, **7**, 4505–4515.

139 Y. Chen and M. W. Kanan, *J. Am. Chem. Soc.*, 2012, **134**, 1986–1989.

140 F. Li, M. Xue, J. Li, X. Ma, L. Chen, X. Zhang, D. R. MacFarlane and J. Zhang, *Angew. Chem., Int. Ed.*, 2017, **56**, 14718–14722.

141 B. Wei, Y. Xiong, Z. Zhang, J. Hao, L. Li and W. Shi, *Appl. Catal., B*, 2021, **283**, 119646.

142 H. Li, T. Liu, P. Wei, L. Lin, D. Gao, G. Wang and X. Bao, *Angew. Chem., Int. Ed.*, 2021, **60**, 14329–14333.

143 S. Mou, Y. Li, L. Yue, J. Liang, Y. Luo, Q. Liu, T. Li, S. Lu, A. M. Asiri, X. Xiong, D. Ma and X. Sun, *Nano Res.*, 2021, **14**, 2831–2836.

144 S. Sarfraz, A. T. Garcia-Esparza, A. Jedidi, L. Cavallo and K. Takanabe, *ACS Catal.*, 2016, **6**, 2842–2851.

145 D. Li, L. Huang, Y. Tian, T. Liu, L. Zhen and Y. Feng, *Appl. Catal., B*, 2021, **292**, 120119.

146 B. Qiao, A. Wang, X. Yang, L. F. Allard, Z. Jiang, Y. Cui, J. Liu, J. Li and T. Zhang, *Nat. Chem.*, 2011, **3**, 634–641.

147 M. Wang, M. Li, Y. Liu, C. Zhang and Y. Pan, *Nano Res.*, 2022, **15**, 4925–4941.

148 Q. Sun, C. Jia, Y. Zhao and C. Zhao, *Chin. J. Catal.*, 2022, **43**, 1547–1597.

149 B. Mohanty, S. Basu and B. K. Jena, *J. Energy Chem.*, 2022, **70**, 444–471.

150 H. Yang, Y. Wu, G. Li, Q. Lin, Q. Hu, Q. Zhang, J. Liu and C. He, *J. Am. Chem. Soc.*, 2019, **141**, 12717–12723.

151 K. Zhao, X. Nie, H. Wang, S. Chen, X. Quan, H. Yu, W. Choi, G. Zhang, B. Kim and J. G. Chen, *Nat. Commun.*, 2020, **11**, 2455.

152 Y. Cai, J. Fu, Y. Zhou, Y. C. Chang, Q. Min, J. J. Zhu, Y. Lin and W. Zhu, *Nat. Commun.*, 2021, **12**, 586.

153 Y. Wang, Z. Chen, P. Han, Y. Du, Z. Gu, X. Xu and G. Zheng, *ACS Catal.*, 2018, **8**, 7113–7119.

154 H. Bao, Y. Qiu, X. Peng, J. A. Wang, Y. Mi, S. Zhao, X. Liu, Y. Liu, R. Cao, L. Zhuo, J. Ren, J. Sun, J. Luo and X. Sun, *Nat. Commun.*, 2021, **12**, 238.

155 Q. Zhao, C. Zhang, R. Hu, Z. Du, J. Gu, Y. Cui, X. Chen, W. Xu, Z. Cheng, S. Li, B. Li, Y. Liu, W. Chen, C. Liu, J. Shang, L. Song and S. Yang, *ACS Nano*, 2021, **15**, 4927–4936.

156 Y. Jiao, Y. Zheng, P. Chen, M. Jaroniec and S.-Z. Qiao, *J. Am. Chem. Soc.*, 2017, **139**, 18093–18100.

157 S. Chen, B. Wang, J. Zhu, L. Wang, H. Ou, Z. Zhang, X. Liang, L. Zheng, L. Zhou, Y.-Q. Su, D. Wang and Y. Li, *Nano Lett.*, 2021, **21**, 7325–7331.

158 M. Naguib, V. N. Mochalin, M. W. Barsoum and Y. Gogotsi, *Adv. Mater.*, 2014, **26**, 992–1005.

159 J.-C. Lei, X. Zhang and Z. Zhou, *Front. Phys.*, 2015, **10**, 276–286.

160 J. Zhu, M. Xiao, D. Ren, R. Gao, X. Liu, Z. Zhang, D. Luo, W. Xing, D. Su, A. Yu and Z. Chen, *J. Am. Chem. Soc.*, 2022, **144**, 9661–9671.

161 Y. Ouyang, L. Shi, X. Bai, Q. Li and J. Wang, *Chem. Sci.*, 2020, **11**, 1807–1813.

162 Z. Liang, C. Qu, W. Guo, R. Zou and Q. Xu, *Adv. Mater.*, 2018, **30**, 1702891.

163 R. Hinogami, S. Yotsuhashi, M. Deguchi, Y. Zenitani, H. Hashiba and Y. Yamada, *ECS Electrochem. Lett.*, 2012, **1**, H17.

164 L. Majidi, A. Ahmadiparidari, N. Shan, S. N. Misal, K. Kumar, Z. Huang, S. Rastegar, Z. Hemmat, X. Zou, P. Zapol, J. Cabana, L. A. Curtiss and A. Salehi-Khojin, *Adv. Mater.*, 2021, **33**, 2004393.

165 F. Yang, A. Chen, P. L. Deng, Y. Zhou, Z. Shahid, H. Liu and B. Y. Xia, *Chem. Sci.*, 2019, **10**, 7975–7981.

166 L. Wang, X. Li, L. Hao, S. Hong, A. W. Robertson and Z. Sun, *Chin. J. Catal.*, 2022, **43**, 1049–1057.

167 I. U. Din, M. Usman, S. Khan, A. Helal, M. A. Alotaibi, A. I. Alharthi and G. Centi, *J. CO2 Util.*, 2021, **43**, 101361.

168 X.-F. Qiu, H.-L. Zhu, J.-R. Huang, P.-Q. Liao and X.-M. Chen, *J. Am. Chem. Soc.*, 2021, **143**, 7242–7246.

169 J. Liu, D. Yang, Y. Zhou, G. Zhang, G. Xing, Y. Liu, Y. Ma, O. Terasaki, S. Yang and L. Chen, *Angew. Chem., Int. Ed.*, 2021, **60**, 14473–14479.

170 Z. Yang, H. Wang, X. Fei, W. Wang, Y. Zhao, X. Wang, X. Tan, Q. Zhao, H. Wang, J. Zhu, L. Zhou, H. Ning and M. Wu, *Appl. Catal., B*, 2021, **298**, 120571.

171 Y. Xue, C. Li, X. Zhou, Z. Kuang, W. Zhao, Q. Zhang and H. Chen, *ChemElectroChem*, 2022, **9**, e202101648.

172 K. Yao, Y. Xia, J. Li, N. Wang, J. Han, C. Gao, M. Han, G. Shen, Y. Liu, A. Seifitokaldani, X. Sun and H. Liang, *J. Mater. Chem. A*, 2020, **8**, 11117–11123.

173 B. Yang, K. Liu, H. Li, C. Liu, J. Fu, H. Li, J. E. Huang, P. Ou, T. Alkayyali, C. Cai, Y. Duan, H. Liu, P. An, N. Zhang, W. Li, X. Qiu, C. Jia, J. Hu, L. Chai, Z. Lin, Y. Gao, M. Miyauchi, E. Cortés, S. A. Maier and M. Liu, *J. Am. Chem. Soc.*, 2022, **144**, 3039–3049.

174 H. Xu, D. Rebollar, H. He, L. Chong, Y. Liu, C. Liu, C.-J. Sun, T. Li, J. V. Muntean, R. E. Winans, D.-J. Liu and T. Xu, *Nat. Energy*, 2020, **5**, 623–632.

175 J. Albo, D. Vallejo, G. Beobide, O. Castillo, P. Castaño and A. Irabien, *ChemSusChem*, 2017, **10**, 1100–1109.

176 K. Zhao, Y. Liu, X. Quan, S. Chen and H. Yu, *ACS Appl. Mater. Interfaces*, 2017, **9**, 5302–5311.

177 J. Albo, M. Perfecto-Irigaray, G. Beobide and A. Irabien, *J. CO2 Util.*, 2019, **33**, 157–165.

178 Z. Weng, Y. Wu, M. Wang, J. Jiang, K. Yang, S. Huo, X.-F. Wang, Q. Ma, G. W. Brudvig and V. S. Batista, *Nat. Commun.*, 2018, **9**, 1–9.

179 M. K. Kim, H. J. Kim, H. Lim, Y. Kwon and H. M. Jeong, *Electrochim. Acta*, 2019, **306**, 28–34.